RSC Sustainability

ROYAL SOCIETY OF CHEMISTRY

PAPER

View Article Online
View Journal | View Issue

Cite this: *RSC Sustainability*, 2026, **4**, 1464

Nanofiltration membranes based on cellulose triacetate from millet husk

Maryam Khadim MBACKE, *[ac] Mouhamed Ndoye,[b] El Hadji Moussa Diop[ab] and Moustapha Sene[d]

This study reports the sustainable fabrication of nanofiltration (NF) membranes based on cellulose triacetate (CTA) derived from millet husk, an abundant and underutilized agricultural residue in Sahelian Africa. Cellulose was extracted, acetylated to a degree of substitution of 2.67, and processed into asymmetric membranes by non-solvent induced phase inversion using contrasting solvents (chloroform and dichloromethane) and glycerol as a benign pore-forming additive. Structural, electrokinetic, and separation analyses reveal that solvent choice governs phase-inversion kinetics, pore size distribution, and surface charge, thereby controlling the permeability–selectivity balance. Chloroform-based membranes exhibit macrovoid-rich morphologies with broader pore size distributions, delivering higher water permeability (9.7 $L \cdot m^{-2} \cdot h^{-1} \cdot bar^{-1}$) while maintaining high divalent-ion rejection (up to 95% for $MgSO_4$). Dichloromethane induces denser skins, narrower pore size distributions, and more negative surface charge, enhancing steric and electrostatic exclusion at the expense of flux. The combined steric and Donnan effects explain the selective rejection of multivalent ions over monovalent salts. This work demonstrates that agro-residue-derived CTA membranes can achieve performance comparable to commercial NF membranes while offering a low-carbon, bio-based alternative, providing a viable pathway toward sustainable water treatment technologies.

Received 27th November 2025
Accepted 15th January 2026

DOI: 10.1039/d5su00889a

rsc.li/rscsus

Sustainability spotlight

This work advances sustainable materials engineering by transforming millet husk—an abundant African agro-residue—into high-performance cellulose triacetate nanofiltration membranes. By valorizing local biomass and reducing dependence on fossil-based polymers, the study supports SDG 12 (Responsible Consumption and Production) and strengthens circular bioeconomy pathways. The membranes demonstrate efficient removal of divalent ions and contaminants, contributing directly to SDG 6 (Clean Water and Sanitation) through low-pressure, energy-efficient treatment solutions. The use of local feedstocks and environmentally conscious processes also promotes SDG 13 (Climate Action) by lowering carbon footprints and encouraging sustainable resource management. Overall, this research provides a scalable, eco-friendly alternative for water purification in developing regions.

1. Introduction

Nanofiltration, a pressure-driven membrane process, has emerged as a critical technology for water purification, wastewater treatment, and resource recovery, bridging the gap between ultrafiltration and reverse osmosis. Operating within a pore size range of 1–10 nanometers, nanofiltration membranes selectively remove multivalent ions, organic micropollutants, and nanoparticles while allowing monovalent ions and water molecules to permeate.[1] This selective permeability is largely attributed to both size exclusion and Donnan equilibrium effects, enabling efficient separation of electrolyte solutions based on ion valence and hydrated ionic radii.[2] Despite these advantages, widespread application of nanofiltration is often hindered by membrane fouling, which significantly reduces flux and separation efficiency due to the adsorption and deposition of contaminants on the membrane surface or within its pores.[3,4] Consequently, the development of fouling-resistant membranes remains a paramount challenge in advancing nanofiltration technology for sustainable water treatment solutions. Previous studies have investigated the preparation of nanofiltration and related membranes from lignocellulosic residues and biomass-derived celluloses, including agricultural by-products and non-wood plant materials, as sustainable alternatives to conventional petroleum-based polymers.[5–7] Cellulose acetate membranes derived from renewable lignocellulosic feedstocks have shown considerable

[a]*Laboratory of Water, Energy, Environment and Industrial Processes (LE3PI), Polytechnic School, Cheikh Anta Diop University, BP 5085, Dakar, Senegal. E-mail: maryam.mbacke@uam.edu.sn; Tel: +221775745904*

[b]*School of Industrial and Biological Engineering (ESGIB), Dakar, Senegal*

[c]*Laboratory of Sciences, Advanced Technologies and Sustainable Development (LSTADD), Amadou Mahtar Mbow University, Dakar, Senegal*

[d]*Sen Engineering International S.A. 21, Immorama Bulging 2nd Floor, Hann Maristes, Senegal*

promise due to their biodegradability, tunable properties, and relatively low environmental impact.[8,9] However, the literature consistently reports several limitations, notably the variability in cellulose purity and degree of substitution associated with heterogeneous biomass sources, which leads to poor reproducibility of membrane performance.[5,10] In addition, strong hydrogen bonding within cellulose-based matrices often results in dense or collapsed structures with limited pore interconnectivity, reducing permeability, while swelling and fouling remain major challenges affecting long-term stability.[11–14]

To overcome these limitations, several membrane functionalisation strategies have been proposed in the literature, including polymer blending, surface modification, and the incorporation of bio-based or inorganic nanofillers. The introduction of functional additives such as cellulose nanocrystals, nanofibers, or graphene-based materials has been shown to improve pore structure regulation, mechanical stability, hydrophilicity, and antifouling behaviour by modulating surface charge density and reducing surface roughness.[15–17] Surface functionalisation approaches, including controlled acetylation, sulfonation, or the grafting of hydrophilic functional groups, have also been reported to mitigate swelling and enhance selectivity by tailoring membrane–solute interactions.[8,18]

In this context, the use of millet husk as a lignocellulosic feedstock offers several strategic advantages to address these challenges. Millet husk is an abundant, low-cost, and underutilized agricultural residue, particularly in semi-arid regions; its high characterized by a high cellulose content and the limited number of established valorisation pathways make it an attractive and sustainable feedstock for membrane fabrication. Its availability and relatively homogeneous composition, when combined with controlled alkaline extraction and acetylation, enable improved control over cellulose purity and degree of substitution, thereby enhancing the reproducibility of membrane properties. Furthermore, valorising millet husk contributes to waste minimisation and circular bioeconomy objectives, while reducing reliance on wood-based or food-competing resources. Building on these advantages and insights from previous studies, the present work implements a controlled conversion of millet husk–derived cellulose into cellulose acetate, coupled with a rational choice of solvents and phase-inversion conditions to steer membrane structural evolution. This integrated approach improves control over membrane architecture and surface properties, mitigates the structural and stability limitations reported in earlier biomass-derived membrane studies, and contributes to the development of more robust and sustainable nanofiltration membranes.

2. Materials and methods

2.1 Chemical profiling of millet husk

The compositional analysis of millet husk was carried out following the general guidelines of the NREL analytical procedure for lignocellulosic biomass (NREL/TP-510-42618). All experiments were performed in duplicate, and the reported values correspond to the mean of the two measurements.

2.2 Alkaline pretreatment of millet husk for cellulose isolation

The millet husk (glumes) used in this study was processed without any mechanical grinding or particle size reduction prior to alkaline treatment. This choice was based on the intrinsic morphology of the glumes, which exhibit a thin, brittle, and naturally open fibrous structure, providing a relatively high surface-to-volume ratio and facilitating the penetration of alkaline solutions into the lignocellulosic matrix. As a result, efficient delignification and hemicellulose removal could be achieved directly during alkaline extraction. Unlike more compact lignocellulosic feedstocks, such as wood chips or densely packed agricultural residues, which commonly require a preliminary grinding or milling step to enhance chemical accessibility, the millet husk allows for a simplified pretreatment route. The alkaline treatment conditions were determined using a statistical optimization approach based on response surface methodology (RSM) implemented with Design-Expert® software (Stat-Ease Inc., USA). A Box–Behnken experimental design was employed to systematically investigate the combined effects of key process parameters, including alkali concentration, treatment temperature, and reaction time, on cellulose extraction efficiency. The selected response variables were related to delignification efficiency and cellulose preservation.

Raw millet husk was first rinsed several times with distilled water to remove dust and loosely bound contaminants, and then oven-dried at 60 °C for 24 h. The dried material was subsequently subjected to alkaline digestion by dispersing it in a 5% (w/v) sodium hydroxide solution using a solid-to-liquid ratio of 1 : 20 (g mL^{-1}). The mixture was heated to 110 °C and maintained under continuous stirring for 1 h to promote the cleavage and solubilization of hemicellulose, lignin, and other alkali-extractable components.

Following the alkaline step, the suspension was vacuum-filtered, and the solid fraction was washed repeatedly with distilled water until neutrality. The partially delignified biomass was then exposed to an oxidative bleaching treatment using a 2% (v/v) sodium hypochlorite solution, previously adjusted to pH 4.5–5.0 with acetic acid. This reaction was conducted at 70 °C for 1 h under stirring to remove the remaining chromophoric lignin structures, yielding a cellulose-rich material.

The choice of NaClO was guided by its high oxidative efficiency toward lignin aromatic structures under mild operating conditions, allowing effective delignification at moderate temperature, short reaction time, and near neutral to slightly alkaline pH. Compared with hydrogen peroxide, which generally requires elevated temperatures, longer treatment durations, strict pH control, and stabilizing additives to achieve comparable lignin removal, NaClO enables a faster and less energy-intensive process. This reduction in processing time and energy demand contributes to lowering the overall environmental footprint of the pretreatment sequence. Moreover, the controlled use of NaClO under mild conditions limits excessive oxidation or depolymerization of cellulose, thereby preserving polymer integrity while improving cellulose purity prior to

acetylation. Overall, the NaClO-based complementary delignification step offers a balanced compromise between efficiency, process simplicity, and environmental sustainability in the preparation of cellulose for membrane fabrication.

After bleaching, the solid was filtered, rinsed with distilled water to eliminate residual reagents, and dried at 60 °C for 24 h. The resulting cellulose was used as the precursor for subsequent chemical and electrochemical acetylation processes.

2.3 Synthesis of cellulose triacetate

The influence of reaction parameters on the degree of substitution (DS) was evaluated based on controlled acetylation experiments performed under well-defined conditions. In the chemical acetylation route, 10 g of purified cellulose were first swollen in 15 mL of glacial acetic acid, followed by the addition of 1 mL of concentrated sulfuric acid (95 wt%) as the catalyst. The mixture was heated under reflux at 80–90 °C for 30 min, after which 15 mL of acetic anhydride was introduced, corresponding to a large molar excess relative to the anhydroglucose units, to promote extensive hydroxyl substitution. The reaction was then maintained at 70 °C for approximately 15 min, until complete dissolution of the cellulose was observed. The crude triacetate was isolated by nonsolvent precipitation in distilled water, washed thoroughly until neutral pH, and dried at 60 °C. The material was then subjected to structural and thermal analyses.

2.4 Membrane preparation

Nanofiltration membranes were fabricated from millet husk–derived cellulose triacetate (CTA) using the non-solvent induced phase inversion (NIPS) route, a widely adopted method for preparing asymmetric polymeric membranes with controllable pore architecture.[8,9,19] In brief, the acetylated polymer (high substitution level; DS close to the triacetate domain) was dissolved in organic solvents of contrasting affinity and volatility (acetone, chloroform, or dichloromethane), and glycerol was incorporated as a plasticizer/hydrophilic pore-forming additive to modulate demixing and final porosity Fig. 1. The resulting casting solution was poured onto a flat plate, spread to form a uniform film, briefly air-exposed (assisted by a suction-driven drying step) to partially evaporate the solvent, and then immersed in a non-solvent bath to trigger precipitation and membrane formation. This approach intentionally couples (i) solvent engineering and (ii) a benign hydrophilic additive (glycerol) to steer skin-layer formation and sublayer morphology. This preparation strategy is consistent with the most established pathways used for cellulose acetate/cellulose triacetate membranes in water treatment, where membrane performance is primarily governed by polymer quality (degree of acetylation/substitution) and by the ternary interactions between polymer–solvent–non-solvent during NIPS.

The membrane preparation conditions were optimized to achieve a balanced nanofiltration performance in terms of permeability, selectivity, and structural stability. A CTA concentration in the range of 15–17 wt% was selected to ensure adequate mechanical integrity while avoiding excessive densification of the selective layer. Glycerol contents of 8–12 wt% (relative to CTA) were identified as optimal to enhance hydrophilicity and porosity without promoting excessive macrovoid formation. Membranes were cast at a wet thickness of 180–220 μm, followed by a controlled air exposure of 25–40 s prior to immersion in a water coagulation bath maintained at 20–23 °C, conditions that promoted reproducible asymmetric structures with limited macrovoids. Optional mild hydrothermal annealing (50–60 °C, 30 min) was used to further stabilize the selective layer and improve ion rejection.

2.5 Fourier transform infrared (FTIR) spectroscopy

Fourier transform infrared (FTIR) spectra of the cellulose triacetate (CTA) samples were collected using an attenuated total reflectance (ATR) configuration equipped with a universal ATR accessory, operating in the mid-infrared region with a KBr beam splitter. Spectra were recorded in absorbance mode and expressed as sample-to-background ratios. Data acquisition was performed over the 4000–600 cm^{-1} spectral range with a step size of 0.5 cm^{-1} (6801 data points) and a spectral resolution of 2 cm^{-1}. Each spectrum corresponded to the co-addition of 8 scans. Baseline correction was applied using a rubber-band

Fig. 1 Alkaline pretreatment route applied to millet husk for cellulose extraction, including washing, alkaline digestion, oxidative bleaching, and recovery of purified cellulose prior to acetylation.

algorithm, followed by vector normalization to enable meaningful comparison of relative band intensities between samples.

2.6 X-ray diffraction (XRD) analysis

X-ray diffraction (XRD) measurements were carried out to probe the structural organisation of cellulose triacetate (CTA) obtained *via* chemical and electrochemical acetylation routes, and to benchmark the results against a commercial CTA reference. Diffraction patterns were recorded using an X'Pert PRO diffractometer operating with Cu Kα radiation ($\lambda = 1.5406$ Å) in θ–θ geometry (PW3050/60 goniometer). Data were collected over a 2θ range of 4.01–74.99° with an angular step of approximately 0.013° 2θ (5407 data points).

The raw diffractograms were baseline-corrected and deconvoluted to discriminate the contribution of the broad amorphous halo, typically centred between 8 and 10° 2θ, from the pseudo-crystalline diffraction maximum located around 20–22° 2θ, which is associated with short-range ordered CTA domains. Owing to the predominantly amorphous nature of CTA and the absence of well-defined crystalline reflections, the crystallinity index (CI) was not determined using the classical Segal method. Instead, CI was calculated using an area-based approach derived from peak deconvolution according to:

$$\mathrm{CI} = \frac{A_{\mathrm{cryst}}}{A_{\mathrm{cryst}} + A_{\mathrm{amorph}}} \quad (1)$$

where A_{cryst} and A_{amorph} represent the integrated areas of the pseudo-crystalline and amorphous components, respectively, obtained by Gaussian fitting.

The apparent crystallite size associated with the pseudo-crystalline domain was estimated using the Scherrer equation:

$$L = \frac{K\lambda}{\beta \cos \theta} \quad (2)$$

where $K = 0.9$, $\lambda = 1.5406$ Å, β corresponds to the full width at half maximum (FWHM) of the 20–22° 2θ peak after correction for instrumental broadening (expressed in radians), and θ is the Bragg angle. This analysis provides a consistent description of short-range molecular ordering and highlights subtle differences in chain packing induced by the acetylation pathway.

2.7 Thermogravimetric analysis (TGA/DTG)

Thermal stability and decomposition behaviour of the CTA samples were evaluated by thermogravimetric analysis (TGA) using a PerkinElmer Pyris TGA analyser. Both TGA (mass loss *versus* temperature) and derivative thermogravimetric (DTG) curves were recorded to determine the characteristic degradation temperatures (T_onset, T_max and T_endset) as well as the final residue content.

Approximately 9.6 mg of CTA produced *via* chemical and electrochemical acetylation and 15.4 mg of commercial CTA were analysed. All samples were in the form of homogeneous fine powders and were pre-dried at 60 °C under vacuum for 12 h to remove residual moisture. Measurements were conducted under a controlled dual-atmosphere programme. An initial inert phase under nitrogen (N_2, 100 mL·min^{-1}) was applied to monitor pyrolysis and primary thermal decomposition, followed by an oxidising phase under air (100 mL·min^{-1}) to ensure complete combustion of the carbonaceous residue and to assess oxidative stability. Gas flow rates were regulated by a mass-flow controller integrated into the instrument.

The temperature programme consisted of a linear heating ramp from 25 to 500 °C at 5 °C·min^{-1} under nitrogen, followed by a 15 min isothermal hold at 500 °C prior to switching to air. Alumina (Al_2O_3) crucibles were used owing to their high thermal stability and chemical inertness and were calibrated before each experiment to ensure accurate mass measurements. T_onset was determined using the tangent-intersection method in accordance with ISO 11358, T_max was defined as the temperature corresponding to the maximum of the DTG peak, and T_endset was identified as the temperature at which the TGA curve reached a stable plateau after the main decomposition event.

2.8 Permeability and stability tests

Pure-water permeability and stability tests were carried out in a flat-sheet crossflow filtration cell with an effective membrane area of $A = 16$ cm^2 (unless otherwise stated). The feed solution consisted of deionized water with a conductivity below 10 μS·cm^{-1}, and the temperature was maintained at 25 ± 1 °C throughout all experiments. The crossflow velocity was fixed at 0.25 m·s^{-1}, to minimize concentration polarization effects. Prior to permeability measurements, membranes were preconditioned to ensure stable and reproducible hydraulic behavior. Each membrane was first rinsed with deionized water for 30 min without applied pressure, followed by a precompaction step at 10 bar for 30–45 min until the flux variation was less than 1% over 10 min. Water permeability was then evaluated under stepwise increasing transmembrane pressures of 2, 4, 6, 8, 10, 12, 15, and 16 bar. At each pressure step, the system was allowed to stabilize for 20 min, and the steady-state flux was calculated from the average permeate volume collected during the final 5–10 min. Membrane hydraulic stability was further assessed through long-term filtration experiments conducted at a constant pressure of 15 bar for periods ranging from 8 to 24 h, during which the permeate flux was continuously monitored at regular intervals of 10–30 min.

3. Results and discussion

3.1 Characterization of millet husk

The chemical composition of millet husk was determined to assess its suitability as a source of cellulose for membrane synthesis. The analysis revealed that the husk contained 31.45% cellulose, 28.54% hemicellulose, and 8.7% lignin. The relatively high cellulose fraction indicates that millet husk can serve as a promising feedstock for cellulose derivatives, particularly for the development of sustainable membranes. In comparison, rice husk and corn stover typically contain cellulose contents in the range of 28–35% and 32–38%, respectively, while sugarcane bagasse often exceeds 40%.[20–22] Thus, the cellulose yield of

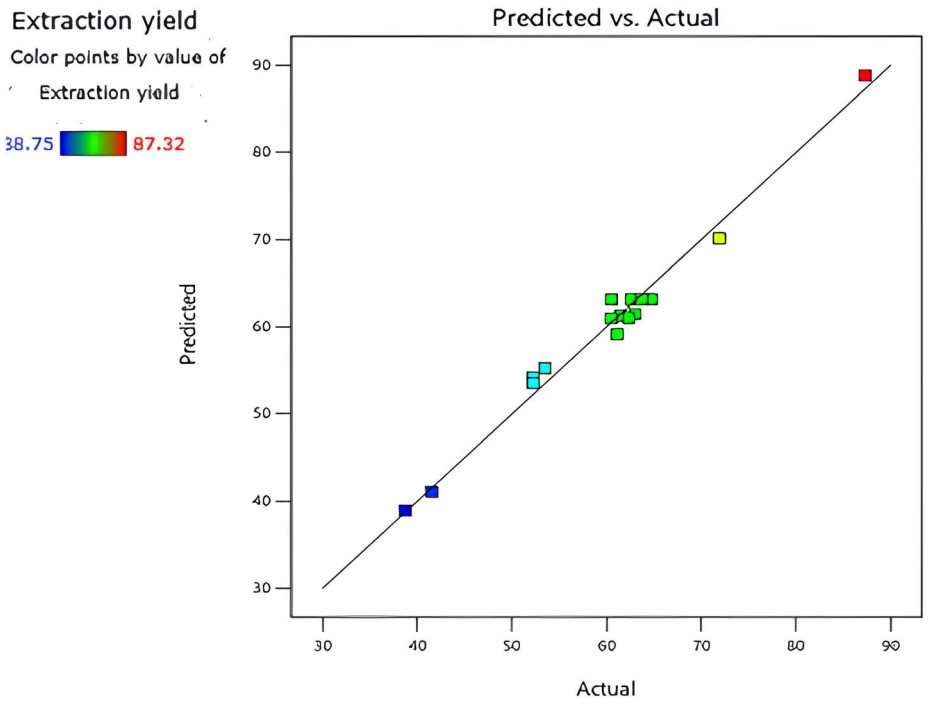

Fig. 2 Correlation between experimental and predicted cellulose extraction yields obtained from the quadratic response surface methodology (RSM) model, showing good agreement and model adequacy.

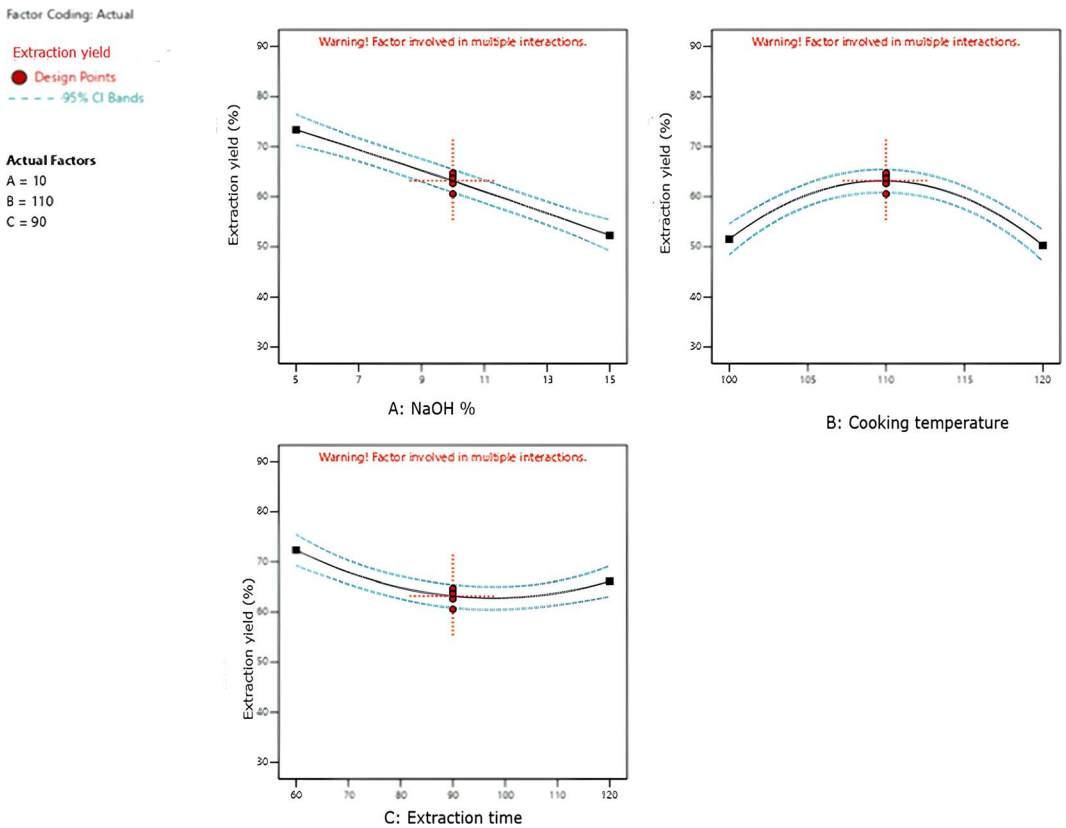

Fig. 3 Main effects of NaOH concentration, cooking temperature, and extraction time on cellulose extraction yield, derived from the Box–Behnken experimental design.

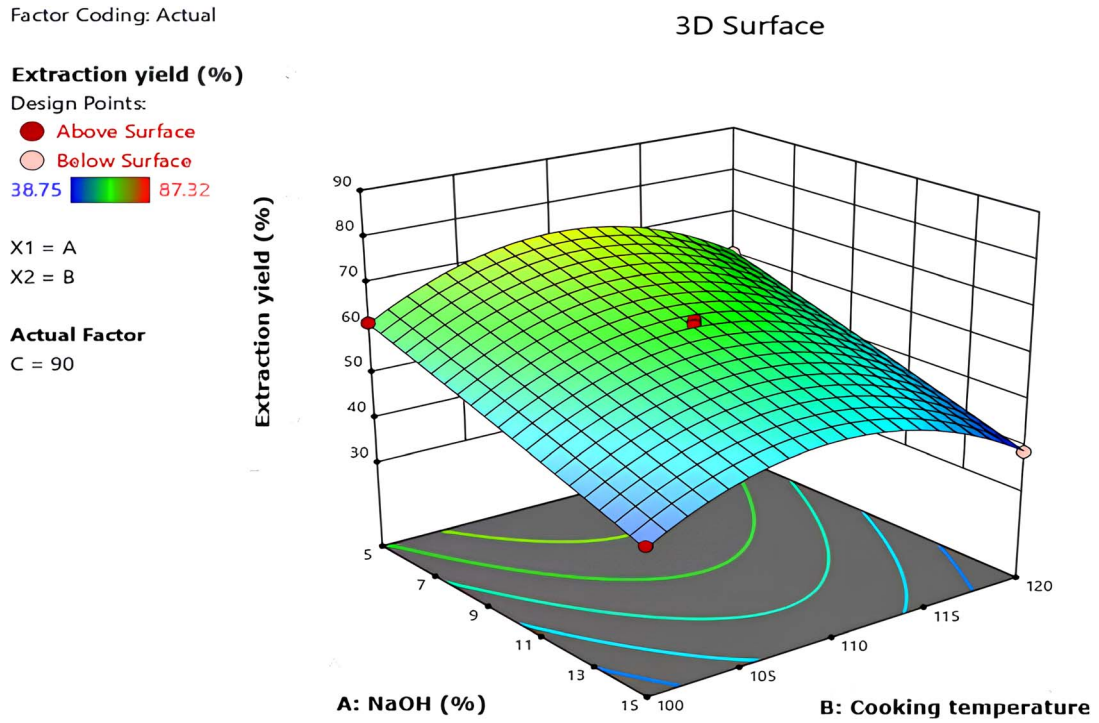

Fig. 4 Response surface plot illustrating the combined effect of cooking temperature and NaOH concentration on cellulose extraction yield.

millet husk is comparable to that of widely studied agro-residues, reinforcing its valorization potential.

The hemicellulose content of 28.54% is within the typical range reported for cereal residues, such as rice husk (20–25%) and corn stover (25–30%), suggesting similar structural heterogeneity and the need for effective pretreatment strategies to facilitate cellulose accessibility.[23,24] The lignin fraction of 8.7% is significantly lower than that of rice husk (15–20%) or sugarcane bagasse (18–24%), which is advantageous since lower lignin content reduces the severity of delignification and may lower chemical and energy requirements during processing.[20–25] These compositional features confirm that millet husk is a competitive and underexploited lignocellulosic resource, providing a sufficiently rich cellulose fraction with relatively low lignin content for membrane synthesis. To validate this potential, the next step focused on extracting and chemically modifying the cellulose through acetylation.

3.2 Optimization of alkaline treatment parameters

The optimization of alkaline treatment conditions for cellulose extraction from millet husk was carried out using a response surface methodology (RSM) coupled with a Box–Behnken experimental design, implemented through Design-Expert® software. Three critical operational parameters—NaOH concentration, cooking temperature, and extraction time—were selected in view of their well-documented effects on lignocellulosic delignification and cellulose swelling behavior. A total of 17 experiments, including five center points, were conducted to evaluate both the individual and interactive effects of these factors on cellulose extraction yield. Statistical analysis demonstrated that a quadratic model adequately described the system, with a high coefficient of determination ($R^2 \approx 0.98$) and a non-significant lack of fit, confirming the robustness and predictive capability of the model. Analysis of variance (ANOVA) revealed that NaOH concentration was the most influential parameter, followed by extraction time, while temperature exhibited a secondary but nonlinear effect. The experimental data were well described by a quadratic model with high predictive accuracy, as evidenced by the strong agreement between experimental and predicted yields (Fig. 2) and a non-significant lack of fit. Among the studied variables, NaOH concentration was identified as the dominant factor, followed by extraction time, while temperature exhibited a secondary but nonlinear effect (Fig. 3).

The three-dimensional response surface plots (Fig. 4, Fig. 5 and Fig. 6) reveal that maximum cellulose recovery is achieved at low alkali concentrations and moderate temperatures, particularly for short extraction times, highlighting a synergistic interaction between NaOH concentration and extraction time.

The optimal conditions, determined using a desirability-based approach (Fig. 7), correspond to approximately 5% NaOH, 110 °C, and 60 min, yielding a maximum cellulose recovery of about 87%.

This statistically guided optimization reduces chemical and energy inputs while maintaining high extraction efficiency, supporting the sustainable valorization of millet husk as a bio-based cellulose source.

3.3 Cellulose extraction and acetylation

Cellulose was isolated from millet husk by alkaline treatment (5% NaOH, 110 °C), a common delignification step that removes most hemicellulose/lignin while preserving the

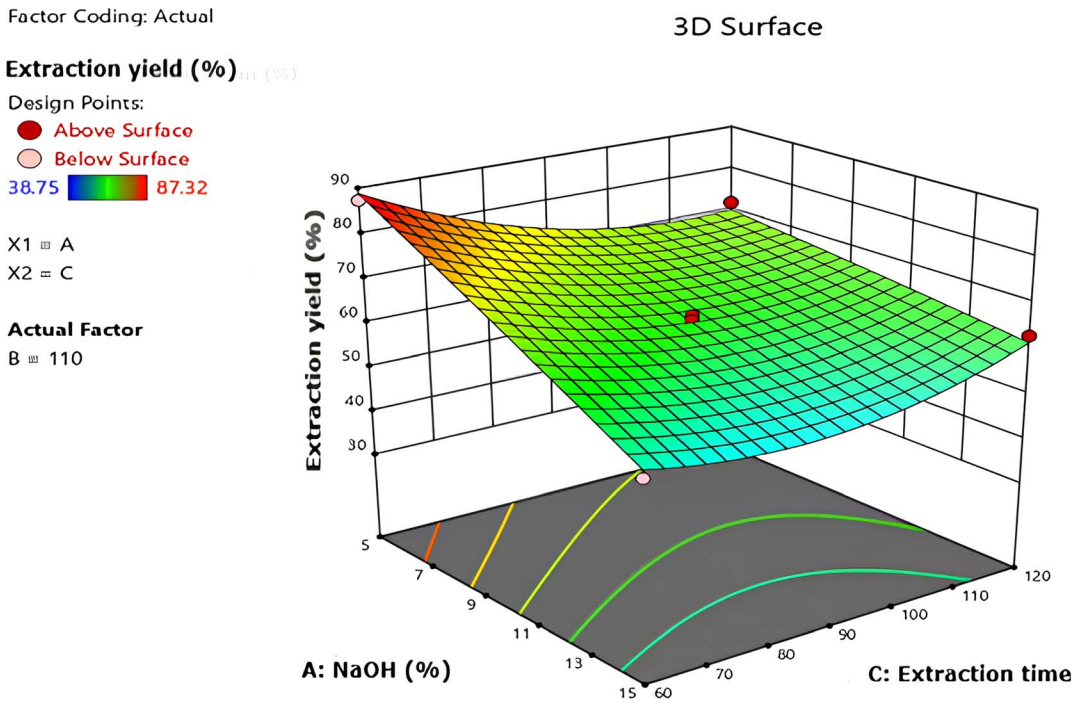

Fig. 5 Response surface plot illustrating the combined effect of NaOH concentration and extraction time on cellulose extraction yield.

polysaccharide backbone and accessibility of surface –OH groups for derivatization. The purified cellulose was then acetylated to obtain cellulose triacetate (CTA) by substituting the C2/C3/C6 hydroxyls with acetyl functional groups, which increases hydrophobicity and organic-solvent affinity—attributes sought for membrane fabrication. Comparable extraction and acetylation routes from low-cost biomass have been reported for date-palm residues, cocoa-pod husk, rice husk, and luffa fibers.[25]

The FTIR spectra in Fig. 8 corroborate this conversion. The cellulose shows a broad O–H stretching envelope at 3330–3500 cm^{-1}, which markedly collapses after acetylation, indicating consumption of accessible hydroxyls. In CTA, intense

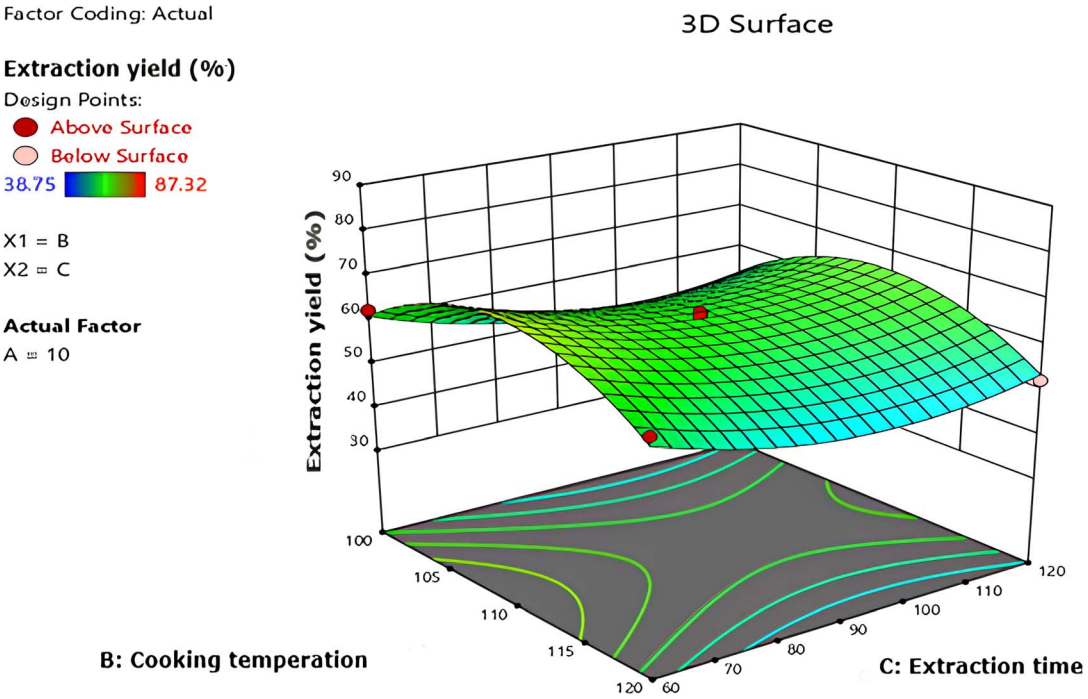

Fig. 6 Response surface plot showing the interaction between extraction time and cooking temperature.

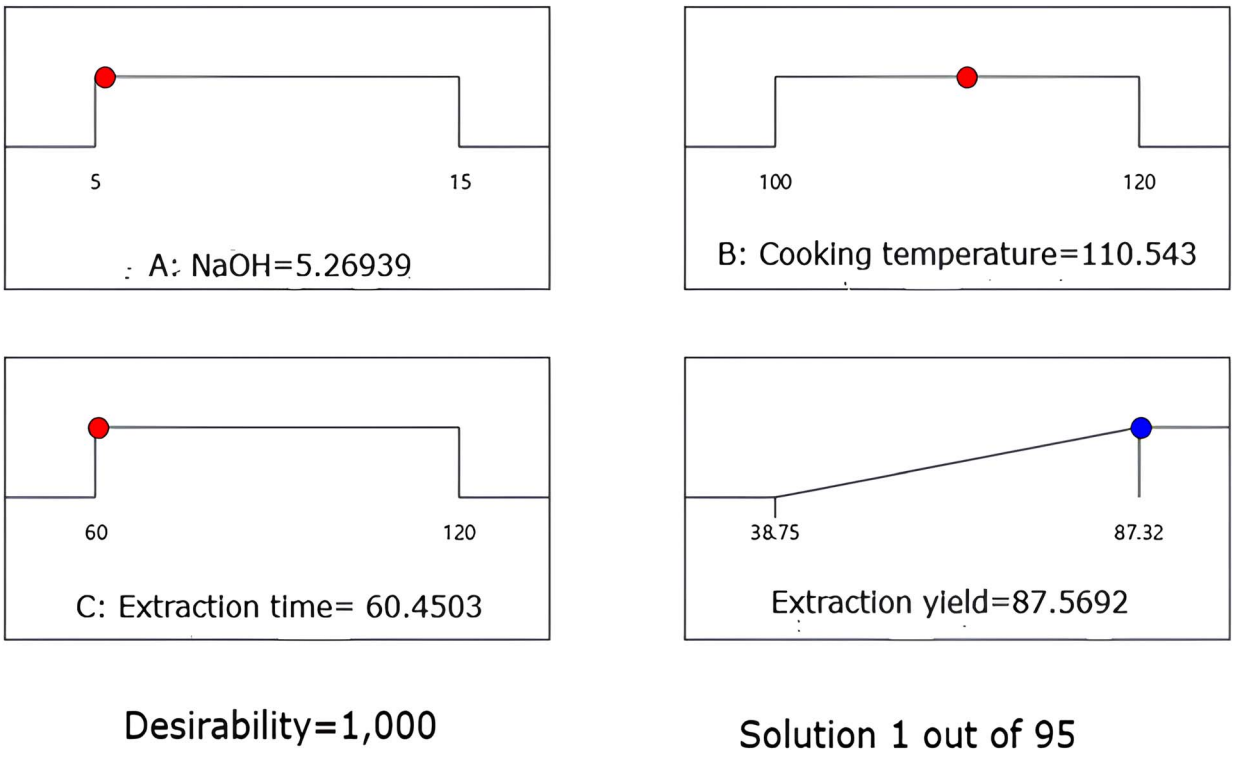

Fig. 7 Desirability function plot identifying the optimal alkaline treatment conditions for cellulose extraction from millet husk.

ester bands appear at ~1735 cm^{-1} ($\nu C=O$) and 1240 cm^{-1} ($\nu C–O–C$ of acetate), accompanied by signals in the fingerprint region (*e.g.*, 1030–1050 cm^{-1} glycosidic C–O) and the CH_3 deformation near 1370 cm^{-1}, all consistent with cellulose triacetate. A faint residual O–H shoulder persisting in CTA suggests that the substitution is high but not exhaustive (DS < 3), likely due to steric/transport limitations in less accessible domains—behavior widely reported for acetylation of lignocellulosic celluloses. Several published studies support the interpretation that a weak residual O–H band/shoulder in the FTIR spectrum of cellulose acetate is consistent with high but incomplete acetylation (DS < 3), especially when cellulose

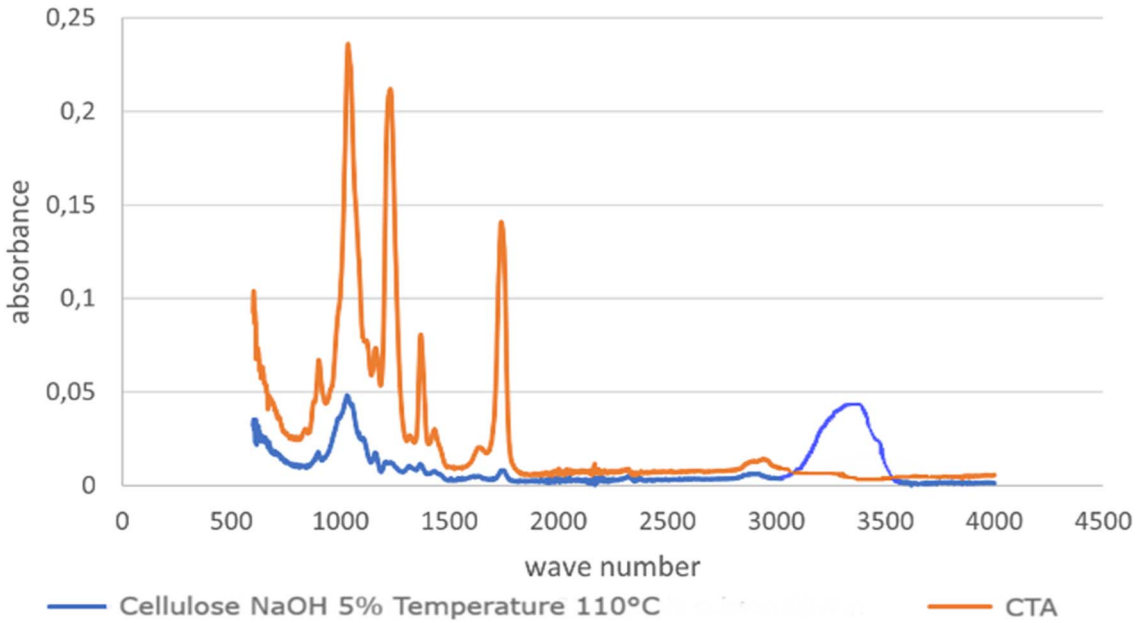

Fig. 8 FTIR spectra of alkali-treated cellulose and synthesized cellulose triacetate (CTA), highlighting the attenuation of the O–H stretching band and the emergence of characteristic ester carbonyl (~1740 cm^{-1}) and C–O–C stretching bands, confirming successful acetylation.

originates from lignocellulosic biomass. In most "conventional" acetylation routes (acetic anhydride/acetic acid with acid catalysis), FTIR typically shows a strong ester C=O band (~1740–1750 cm^{-1}) while the broad O–H band (~3200–3600 cm^{-1}) markedly decreases but may remain detectable, reflecting unreacted hydroxyls in less accessible domains. This behavior aligns with the broader understanding that cellulose accessibility (crystalline *vs.* amorphous regions, fiber wall porosity) can impose diffusion/transport and steric limitations, preventing exhaustive substitution across all three hydroxyls per anhydroglucose unit. In fact, reviews of cellulose acetate note that fully substituted material (DS = 3) is not the most common outcome under standard processing and that DS values around ~2–2.5 are frequently encountered in practice, consistent with residual O–H signatures.[26]

By contrast, reports achieving near-complete substitution (DS = 3) typically rely on highly effective activation/solvation strategies (*e.g.*, specialized solvent systems or ionic-liquid/superbase approaches) that enhance accessibility of otherwise shielded hydroxyls—highlighting that the limiting factor is often not chemistry alone but mass transfer into compact/crystalline domains.[27] This "high DS but not exhaustive" outcome is also widely discussed in the membrane-oriented cellulose acetate literature, where FTIR-detected residual O–H is commonly linked to incomplete substitution and structural heterogeneity inherent to biomass-derived celluloses.[8]

The spectral evolution mirrors reports where disappearance of the O–H band and emergence of strong 1735/1240 cm^{-1} ester features signpost successful acetylation of biomass-derived cellulose to CTA/CA. For CTA synthesized from date-palm waste, the same diagnostic carbonyl and acetate C–O–C bands were observed; cocoa-pod husk CTA shows identical markers after NaOH extraction and peroxide bleaching; ultrasound-assisted acetylation of rice-husk cellulose yields equivalent FTIR fingerprints; and luffa-derived cellulose acetate membranes display the characteristic ester peaks while the O–H band is strongly suppressed.[25] Together these analogs support both our extraction efficacy and the high acetylation level inferred from Fig. 8. Semi-quantitative DS can be estimated. Using the ATR-FTIR band-area proxy A_{1735}/A_{1030}, we obtain a ratio of ~1.5 from Fig. 8, which—under standard ATR-FTIR calibrations for cellulose acetates—corresponds to an apparent degree of substitution of about 2.7 ± 0.2 (*i.e.*, very close to the triacetate limit, DS = 3). The degree of acetylation (DA) of acetylated cellulose was also determined by acid–base titration (DS = 2.67).

Successful conversion of cellulose into cellulose triacetate, confirmed by FTIR signatures and degree of substitution values, provided the necessary polymer matrix for membrane casting. Attention was then turned to the influence of solvent choice during phase inversion, a parameter known to govern both membrane morphology and performance.

3.4 Thermal behaviour of cellulose triacetate

The thermal stability of chemically acetylated cellulose triacetate (CTA) was evaluated by thermogravimetric (TGA) and derivative thermogravimetric (DTG) analyses (Fig. 9). CTA shows a very limited mass loss below 120 °C (3–5 wt%), which is assigned to the release of physically adsorbed moisture and trace residual volatiles. This behaviour is consistent with the FTIR spectrum, where the broad O–H stretching band at 3200–3600 cm^{-1} is strongly attenuated compared to alkali-treated cellulose, indicating a reduced hydroxyl content because of acetylation.

The main degradation occurs in a single step between approximately 260 and 380 °C, with an onset degradation temperature (T_onset) of 300.1 °C and a maximum mass loss rate (T_max) centered at 327.2 °C. The presence of a single dominant DTG peak contrasts with the multi-step thermal degradation typically observed for native cellulose and reflects

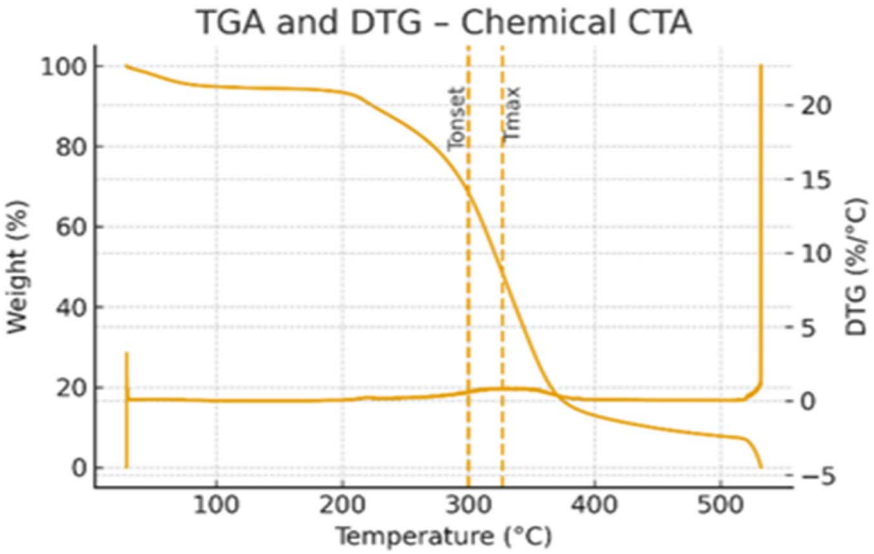

Fig. 9 Thermogravimetric (TGA) and derivative thermogravimetric (DTG) curves of synthesized cellulose triacetate, showing enhanced thermal stability and a single dominant degradation step compared to native cellulose.

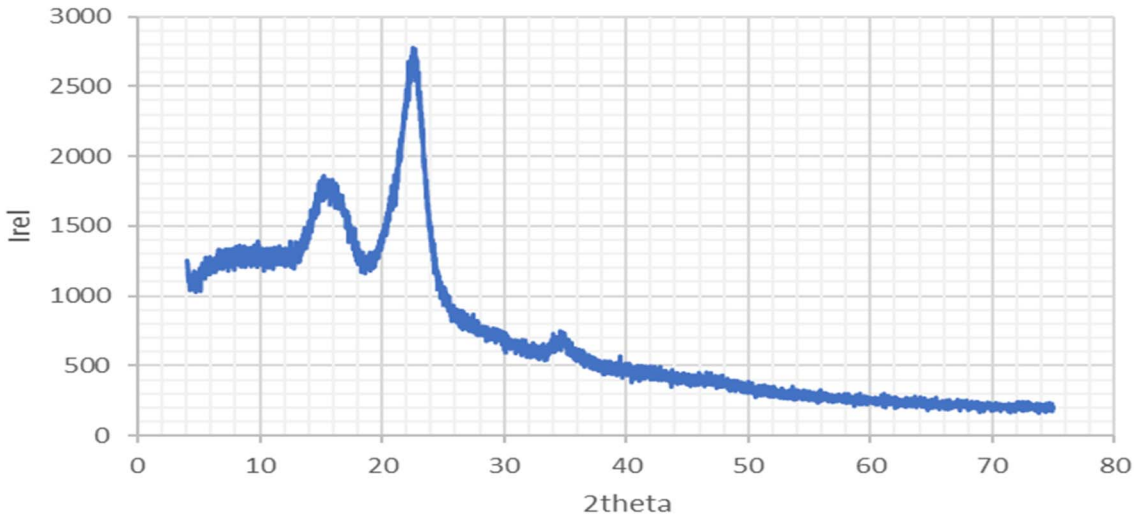

Fig. 10 X-ray diffraction (XRD) pattern of cellulose triacetate, revealing a predominantly amorphous structure with residual short-range ordering following acetylation.

the more homogeneous chemical environment induced by acetyl substitution. This thermal response correlates well with FTIR features characteristic of cellulose triacetate, notably the intense ester carbonyl stretching band at 1740 cm^{-1} and the C–O–C stretching vibrations in the 1210–1030 cm^{-1} region, which confirm extensive esterification of the cellulose backbone.

The upward shift of both T_onset and T_max relative to alkali-treated cellulose indicates an enhancement of thermal stability upon acetylation. This improvement is attributed to the replacement of hydroxyl groups by acetyl moieties, which modifies intermolecular interactions and alters the degradation pathway. At temperatures above 450 °C, CTA leaves a low residual mass of approximately 0.03 wt%, suggesting limited char formation and a degradation mechanism dominated by volatilisation processes rather than carbonisation.

Taken together, the TGA/DTG and FTIR results provide consistent and complementary evidence of successful cellulose acetylation and demonstrate that chemical modification markedly improves the thermal stability of CTA, a key requirement for its processing and application as a membrane material.

3.5 Characterization by X-ray diffractometry

The crystalline organisation of chemically acetylated cellulose triacetate (CTA) was investigated by X-ray diffraction (XRD) analysis (Fig. 10) and correlated with the structural and thermal features previously identified by FTIR and TGA/DTG. The diffractogram exhibits a dominant diffraction peak centered at $2\theta \approx 22–23°$, accompanied by a broader halo extending from approximately 8 to 30°, indicating a predominantly amorphous structure with residual short-range ordering. This diffraction profile is characteristic of cellulose triacetate and differs markedly from that of native or alkali-treated cellulose, which typically displays sharper reflections associated with cellulose I or II crystalline lattices. The pronounced broadening of the main diffraction feature reflects a disruption of the original cellulose crystalline domains following acetylation. This loss of long-range crystallinity is consistent with FTIR results showing extensive substitution of hydroxyl groups by acetyl functionalities, as evidenced by the strong ester carbonyl band at 1740 cm^{-1} and the attenuation of the O–H stretching region. The steric bulk of acetyl groups hinders inter- and intramolecular hydrogen bonding, thereby limiting chain packing and crystalline reorganisation. This structural amorphisation correlates well with the thermal behaviour observed by TGA/DTG. The presence of a single dominant degradation step and a well-defined DTG maximum at 330 °C indicates a more homogeneous degradation pathway, which is typically associated with reduced crystalline heterogeneity. Furthermore, the enhanced thermal stability (higher T_onset and T_max compared to alkali-treated cellulose) suggests that, despite reduced crystallinity, acetylation stabilises the polymer through chemical modification rather than through crystalline reinforcement.

Overall, the XRD results confirm that acetylation induces a transition from an ordered cellulose structure toward a predominantly amorphous CTA matrix. When considered alongside FTIR and TGA/DTG analyses, these findings demonstrate that the chemical substitution of hydroxyl groups governs both the structural organisation and the thermal response of CTA, which is advantageous for membrane processing where uniformity and thermal robustness are required.

Based on a two-Gaussian deconvolution of the broad diffraction halos observed at 8–10° and 20–22°, the cellulose triacetate (CTA) displayed a crystallinity index (CI) of 15.68% and an average crystallite size of 20.36 Å (2.04 nm).

3.6 Effect of solvent on membrane molecular composition

The nanofiltration membranes were prepared using the phase inversion method, a well-established technique for fabricating asymmetric polymeric membranes with tailored pore

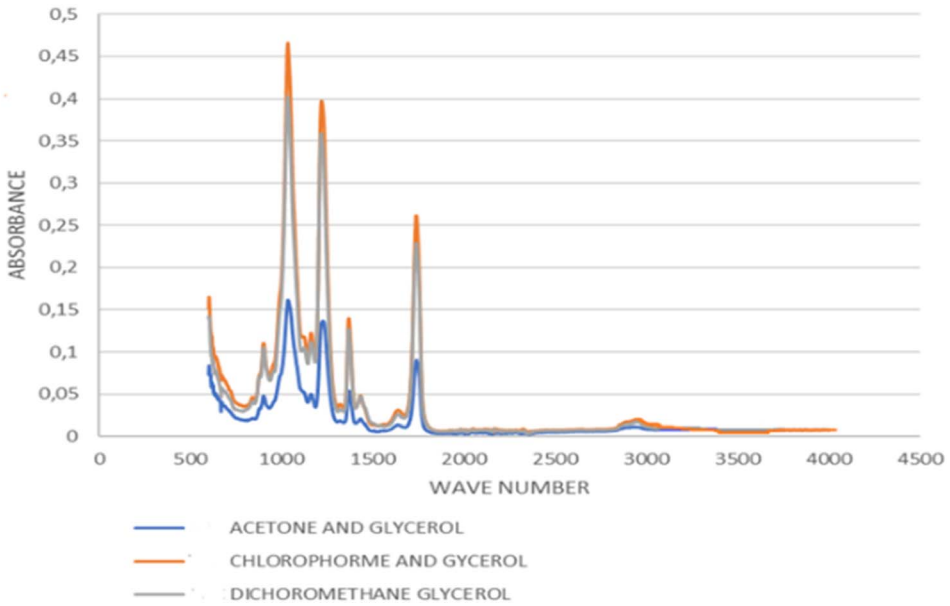

Fig. 11 FTIR spectra of CTA membranes prepared using different solvent–glycerol systems, illustrating solvent-dependent variations in ester and hydroxyl band intensities after baseline correction and internal normalization.

structures. In this process, cellulose triacetate (CTA) synthesized from millet husk cellulose was dissolved in different organic solvents (acetone, chloroform, and dichloromethane) in the presence of glycerol as a plasticizer, followed by casting and immersion in a nonsolvent bath to induce demixing and membrane formation. The choice of solvent significantly affects the polymer–solvent–nonsolvent interactions, thereby influencing the final morphology, porosity, and performance of the membranes. The FTIR spectra of the resulting membranes are shown in Fig. 11.

Quantitative analysis reveals a clear and systematic trend across the solvent systems. The acetylation index increases from 3.61 for the acetone–glycerol membrane to 6.07 for the chloroform–glycerol membrane, reaching a maximum value of 6.37 for the dichloromethane–glycerol membrane. Concomitantly, the hydroxyl index decreases from 5.56 to 4.74, indicating a progressive consumption of hydroxyl groups Table 1. These opposite trends provide direct quantitative evidence that the observed FTIR intensity differences originate from variations in acetylation efficiency and effective degree of substitution rather than from artefacts related to membrane thickness or spectral baseline effects. These trends are consistent with the high but non-exhaustive acetylation (DS < 3) discussed in Section 3.3, reflecting steric and transport limitations inherent to lignocellulosic celluloses.

Table 1 Quantitative FTIR indices used to assess acetylation efficiency and substitution degree of cellulose acetate membranes prepared with different solvent–glycerol systems

Membrane (solvent–glycerol system)	$AI_{C=O/CH}$ [a]	$AI_{C=O/CO}$ [b]	$HI_{OH/CH}$ [c]
Acetone–glycerol	3.61	0.44	5.56
Chloroform–glycerol	6.07	0.46	5.11
Dichloromethane–glycerol	6.37	0.46	4.74

[a] $AI_{C=O/CH}$ = Area(1760–1710 cm^{-1})/Area(2960–2870 cm^{-1}), used as a proxy for acetylation efficiency and effective degree of substitution. [b] $AI_{C=O/C-O}$ = Area(1760–1710 cm^{-1})/Area(1060–1000 cm^{-1}), used to confirm ester enrichment relative to the polysaccharide backbone. [c] $HI_{OH/CH}$ = Area(3600–3200 cm^{-1})/Area(2960–2870 cm^{-1}), reflecting the relative amount of residual hydroxyl groups.

All FTIR spectra were baseline-corrected prior to integration and normalized using the ν(CH) band as an internal reference to minimize membrane thickness and ATR-contact effects. Interestingly, these spectral differences are expected to translate into distinct filtration properties. The stronger C=O and C–O–C signals observed in the chloroform- and dichloromethane-cast membranes indicate a higher degree of substitution and a denser polymer network, typically enhancing solute rejection while slightly reducing water permeability. In contrast, the acetone-based membrane, with its lower absorption intensities, is likely to exhibit looser chain packing and higher free volume, potentially leading to improved water flux but lower salt or organic solute rejection.

Overall, the results confirm that chloroform and dichloromethane are more effective solvents for producing structurally robust CTA membranes with stronger characteristic absorption signals and potentially higher selectivity, while acetone leads to weaker functional group expression, translating into higher permeability but lower rejection. This finding underscores the importance of solvent engineering in tailoring the physicochemical properties of nanofiltration membranes derived from renewable biomass sources, contributing to the broader development of sustainable water treatment technologies.

To better illustrate the correlation between solvent choice, structural organization, and the resulting separation properties, Fig. 12 schematically highlights the expected trade-offs between permeability and selectivity for the different CTA membranes.

Acetone-based membranes show higher water permeability but lower solute rejection due to looser chain packing.

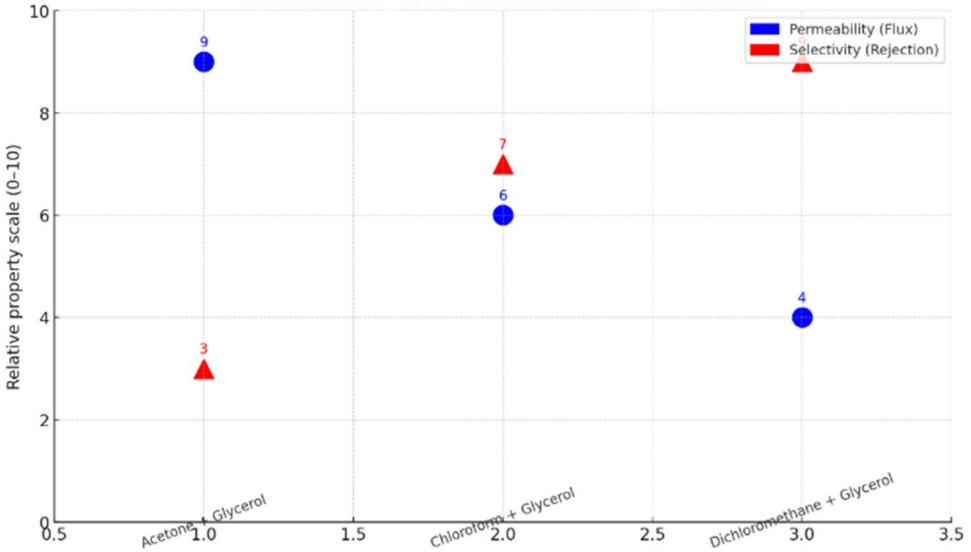

Fig. 12 Schematic illustration of the expected permeability–selectivity trade-off for CTA nanofiltration membranes prepared with different solvents during phase inversion.

Chloroform yields a balanced structure with moderate permeability and good selectivity. Dichloromethane leads to the most compact structure, favoring high solute rejection but at the expense of reduced permeability.

Beyond chemical structure, membrane performance also depends on interfacial electrostatic properties. To this end, the surface charge behavior of the different membranes was investigated by zeta potential measurements.

3.7 Study of zeta potential

The surface charge of the membranes was quantified by electrokinetic measurements in a flat-sheet streaming-potential cell. A dilute, inert electrolyte was circulated tangentially across the active surface while pH was adjusted stepwise with acid/base. The streaming potential ($\Delta E/\Delta P$) was recorded at multiple pressure drops and converted to the zeta potential (ζ) using the Helmholtz–Smoluchowski equation:

$$\zeta = \Delta E/\Delta P \times \frac{\eta}{\varepsilon \kappa} \quad (3)$$

where η is the dynamic viscosity, ε is the dielectric permittivity of water, and κ is the electrolyte conductivity. This approach is standard for polymeric NF/RO membranes and is widely used for cellulose-based films.

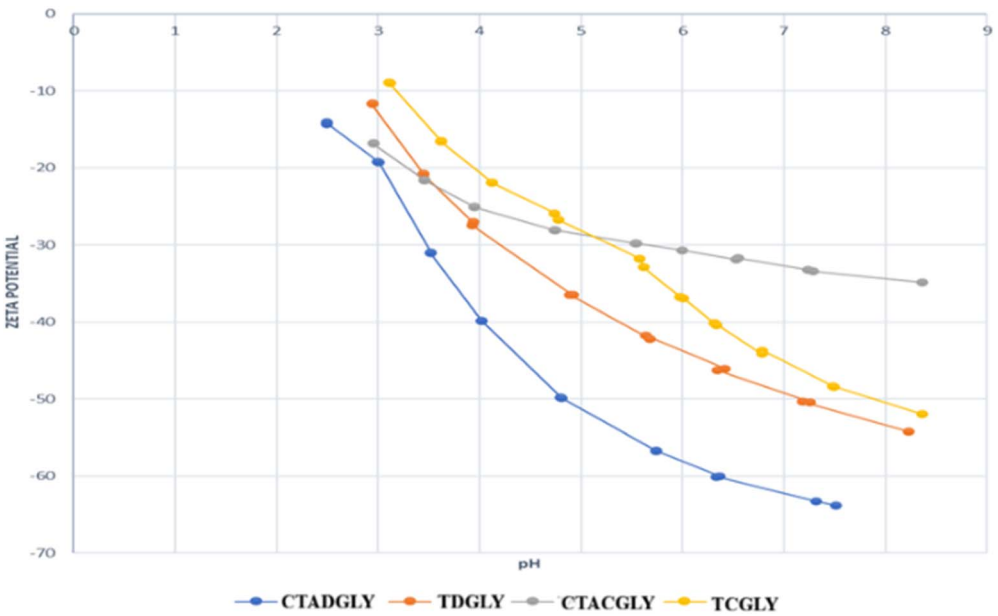

Fig. 13 Zeta potential as a function of pH for CTA membranes prepared from synthesized and commercial CTA using chloroform or dichloromethane, showing solvent- and formulation-dependent surface charge behavior.

Fig. 13 shows that all four membranes are negatively charged over the investigated pH window (~3–8), and their magnitude becomes more negative with increasing pH—consistent with deprotonation of surface hydroxyl/acidic groups on cellulose (acetate) backbones. The apparent isoelectric point lies below pH 3 for every formulation, since ζ is already negative at pH $\approx$ 3. The magnitude and ordering of ζ depend strongly on formulation/processing:

CTA2DGLY exhibits the most negative surface, from ~ -18 mV at pH 3 to ~ -65 mV near pH 7.5–8.

DGLY is moderately negative ($\approx -20 \rightarrow -55$ mV between pH 3–8).

CTA2CGLY shows a milder trend ($\approx -22 \rightarrow -34$ mV between pH 3–6.5).

TCGLY remains the least negative ($\approx -10 \rightarrow -48$ mV between pH 3–8).

CTA2DGLY: membrane obtained from synthesized cellulose triacetate using dichloromethane as solvent.

CTA2CGLY: membrane obtained from synthesized cellulose triacetate using chloroform as solvent.

TDGLY: membrane obtained from commercial cellulose triacetate using dichloromethane as solvent.

TCGLY: membrane obtained from commercial cellulose triacetate using chloroform as solvent.

Together, these profiles show that changing the acetylation/solvent history tunes the density/accessibility of ionizable groups at the interface: the DCM-processed CTA (CTA2DGLY) likely exposes more deprotonatable sites and/or a rougher, more porous skin, while TCGLY remains comparatively less deprotonated. Practically, a more negative ζ at neutral pH should enhance electrostatic repulsion toward anions and negatively charged macromolecules (*e.g.*, NOM and BSA), reducing adsorption/fouling and improving rejection by Donnan exclusion.[8]

The monotonic decrease of ζ with pH matches classic and recent observations on cellulose acetate and other desalination membranes measured by streaming-potential methods. Childress, A.E. showed that ζ becomes increasingly negative with pH and is shifted by solution chemistry; they reported strongly negative ζ for CA and PA films as pH rises.[28] Methodologically, the use of the Helmholtz–Smoluchowski framework and tangential streaming geometry follows the membrane-science canon.[29] Recent reviews on cellulose-based membranes likewise emphasize that ζ becomes more negative with increasing pH and that more negative ζ correlates with

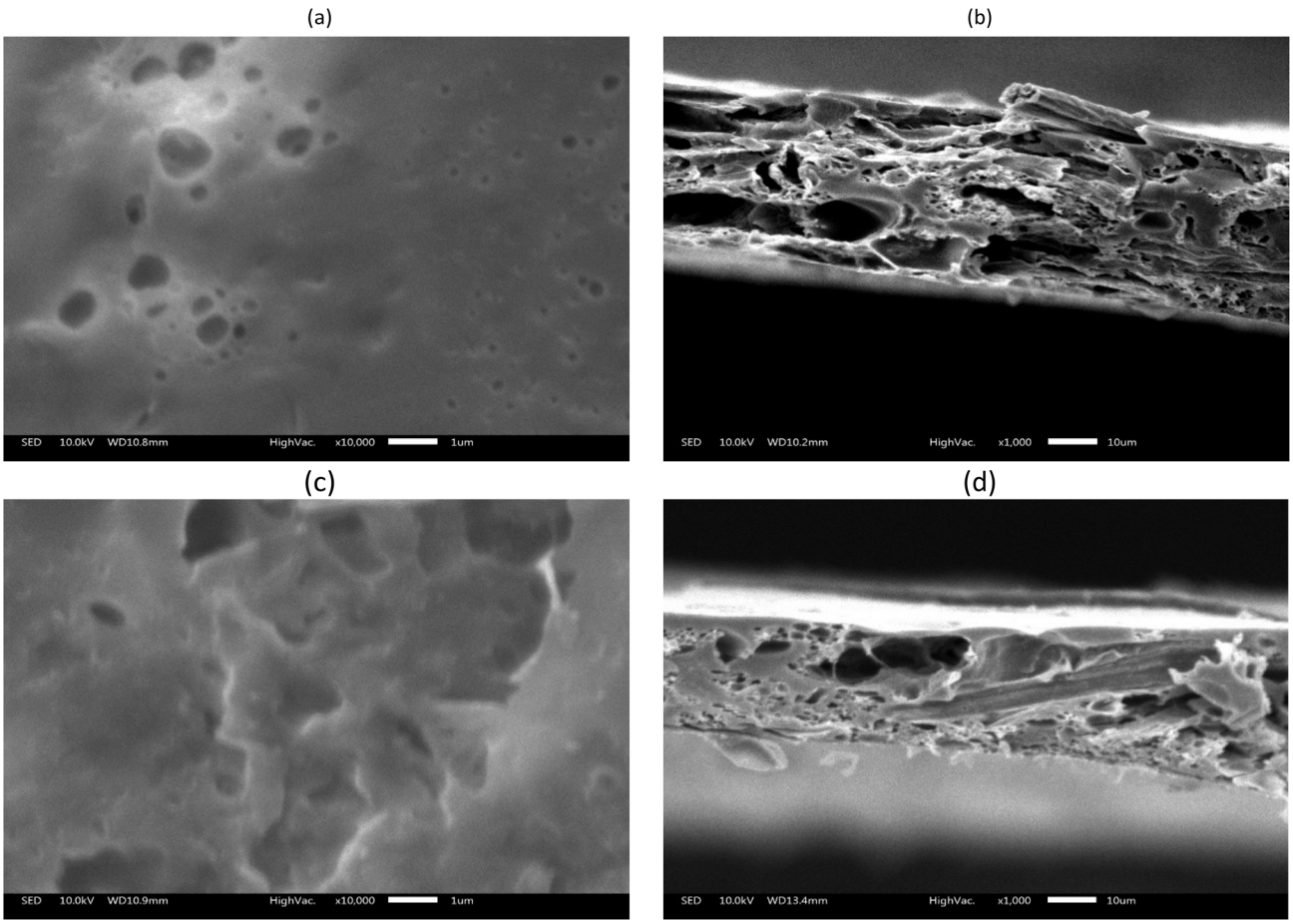

Fig. 14 SEM images of CTA nanofiltration membranes prepared with different solvents: (a and b) CTA2CGLY (chloroform–glycerol) showing a thin selective skin and macrovoid-rich substructure; (c and d) CTA2DGLY (dichloromethane–glycerol) exhibiting a denser skin and more compact substructure. Scale bars and magnifications are indicated.

higher rejection of anionic solutes and reduced fouling—exactly the trend observed here.[8] Moreover, a study on heavy-metal removal with polymeric NF/RO membranes reported negative ζ across the tested pH range and a progressively more negative ζ at higher pH, mirroring our profiles.[30]

Selecting CTA2DGLY (most negative ζ) should favor rejection of anions (*e.g.*, sulfate and chromate) and minimize NOM/BSA adsorption at neutral pH, whereas TCGLY may be preferred when a milder surface charge is needed to limit scaling with multivalent cations. These electrokinetic fingerprints can therefore guide membrane selection and pretreatment (pH set-point and electrolyte) for specific feeds. Since surface charge arises in part from accessible groups exposed at the membrane interface, it was essential to complement electrokinetic data with morphological observations. Scanning electron microscopy was therefore employed to visualize surface and cross-sectional features of the prepared membranes.

3.8 Morphology of the cellulose triacetate membrane

For CTA2CGLY (chloroform, Images a and b), the top surface at 100 00× shows numerous rounded depressions and sub-micrometer pores, while the cross-section (1,000×) is clearly asymmetric with a thin skin over an open, highly porous sublayer containing elongated finger-like cavities and macrovoids interconnected by spongey partitions. In contrast, CTA2DGLY (dichloromethane, Images c and d) exhibits a more compact top surface with fewer and smaller openings and a cross-section whose porous zone is finer and less ramified; occasional voids are present, but the substructure is overall denser than in CTA2CGLY.

These differences are consistent with the well-established coupling between thermodynamics (dope stability) and exchange kinetics during nonsolvent-induced phase inversion. Solvents with slower exchange and higher boiling points can promote delayed demixing in the bulk and stabilize finger-like macrovoids, whereas very fast interfacial exchange can induce early vitrification and a denser skin that suppresses macrovoid growth. The trend we observe—more open, macrovoid-rich substructures with chloroform and a tighter skin/smaller pores with dichloromethane—agrees with reports that solvent identity (diffusivity, viscosity, and affinity for nonsolvent) governs asymmetric morphology in cellulose (acetate/triacetate) systems.[31]

The role of glycerol is also evident. As a water-miscible, hydrophilic additive, glycerol behaves as a weak nonsolvent/pore-forming aid that destabilizes the dope and accelerates solvent–nonsolvent exchange, opening surface pores and increasing sublayer porosity—effects widely documented for hydrophilic pore-formers (including glycerol-based additives) that shift demixing from delayed toward instantaneous and lengthen finger-like channels. This mechanism plausibly explains the visible increase in pore density on CTA2CGLY and, to a lesser extent, on CTA2DGLY.[32]

Chloroform exhibits a higher boiling point (61.2 °C) and higher dynamic viscosity (0.56 mPa·s at 20 °C) compared to dichloromethane (boiling point 39.6 °C; viscosity 0.41 mPa·s). Despite its lower volatility relative to dichloromethane, chloroform shows strong affinity toward cellulose triacetate, as reflected by Hansen solubility parameters, which closely match those of CTA. This strong polymer–solvent interaction facilitates rapid polymer chain expansion in the dope solution and promotes instantaneous liquid–liquid demixing upon immersion in the nonsolvent bath.

Therefore, the CTA2CGLY membrane prepared using chloroform develops a highly porous substructure with elongated finger-like macrovoids and a relatively thin selective skin layer, as observed in Fig. 14b. The broad pore size distribution and extended macrovoids are characteristic of systems where solvent–nonsolvent exchange occurs rapidly, generating localized supersaturation and heterogeneous pore growth.

In contrast, dichloromethane is characterized by higher volatility, lower viscosity, and slightly weaker polymer–solvent

Table 2 Coupling between dope solution properties, phase inversion behavior, and resulting membrane morphology for CTA membranes prepared with chloroform and dichloromethane (with glycerol additive)

Key parameter	CTA2CGLY (chloroform)	CTA2DGLY (dichloromethane)	Morphological implication
Dope solution viscosity at 25 °C (Pa·s)	1.45 ± 0.08	0.92 ± 0.05	Higher viscosity favors rapid supersaturation and macrovoid growth
Solvent boiling point (°C)	61.2	39.6	Lower volatility limits pre-immersion evaporation
Solvent–polymer affinity (Hansen parameter matching)	High	Moderate	Stronger chain expansion *vs.* enhanced interfacial densification
Demixing time, $t_{(demix)}$ (s)	0.8 ± 0.1	2.4 ± 0.3	Instantaneous *vs.* delayed liquid–liquid demixing
Critical water volume fraction at binodal, Φ_v,crit (−)	0.19 ± 0.02	0.27 ± 0.03	Lower thermodynamic stability *vs.* enhanced dope stability
Dominant substructure (SEM)	Finger-like macrovoids	Sponge-like matrix	Convective *vs.* diffusion-limited pore formation
Mean surface pore size (μm)	Larger, broadly distributed	Smaller, narrowly distributed	Permeability- *vs.* selectivity-oriented architecture
Selective skin thickness (μm)	Thin	Thick and uniform	Lower *vs.* higher hydraulic resistance
Expected transport behavior	High permeability	High rejection	Flux-dominated *vs.* selectivity-dominated membrane

Table 3 Quantitative SEM-derived morphological parameters of CTA membranes (Fig. 14)

Membrane	Surface opening diameter (μm)	Macrovoid length (μm)	Skin layer thickness (μm)
CTA2CGLY	0.42 ± 0.15	28 ± 6	0.8 ± 0.2
CTA2DGLY	0.21 ± 0.08	14 ± 4	1.6 ± 0.3

interactions with CTA. Its faster evaporation rate prior to immersion increases the local polymer concentration at the membrane surface, thereby delaying demixing and favoring polymer-rich phase stabilization. Additionally, the reduced affinity between dichloromethane and CTA limits rapid solvent extraction, leading to a more gradual phase inversion process.

This behavior results in the formation of a denser, more uniform sponge-like structure, with shorter macrovoids and a thicker, more homogeneous skin layer, as clearly evidenced in Fig. 14d for the CTA2DGLY membrane. The narrower pore size distribution and suppressed macrovoid growth are consistent with delayed demixing and enhanced polymer chain rearrangement prior to solidification.

Overall, these observations demonstrate that solvent viscosity, volatility, and solubility parameters act synergistically to control the kinetics of phase separation. Chloroform promotes rapid demixing and macrovoid-rich morphologies conducive to high permeability, whereas dichloromethane favors delayed demixing, yielding structurally denser membranes with improved selectivity and mechanical stability. This solvent-dependent morphological tuning provides a robust pathway to optimize the permeability–selectivity trade-off in CTA nanofiltration membranes.

Our observations align with recent literature on cellulose (acetate/triacetate) membranes. Md. D. Islam *et al.* summarized how CA/CTA membranes typically form thin selective skins atop porous supports, with solvent and additive selection dictating whether sponge-like or finger-like substructures dominate.[8] Tekin F. S *et al.* demonstrated that changing the solvent system alone reshapes surface porosity and sublayer architecture in CA membranes *via* shifts in dope viscosity and exchange rates.[33] J. Wang *et al.* similarly emphasize processing–structure–property couplings in cellulose membranes.[9] The present study adds a direct side-by-side comparison for CTA prepared with chloroform *vs.* dichloromethane under otherwise identical conditions with glycerol: chloroform yields a more open, macrovoid-rich architecture beneficial for permeability, while dichloromethane tends to produce a tighter skin that could favor selectivity at the expense of flux.

In glycerol-plasticized CTA systems, solvent selection between chloroform and dichloromethane provides a means of morphology control: chloroform leads to more permeable, macrovoid-rich membranes (CTA2CGLY), while dichloromethane promotes the development of a denser selective layer associated with enhanced selectivity (CTA2DGLY) Table 2. This solvent-tuning approach, previously reported for CA/CTA systems, is applied here specifically to CTA-based nanofiltration membranes, providing a practical means of modulating the flux–rejection balance without altering the polymer chemistry.

3.9 Quantitative SEM analysis of CTA membrane morphology (Fig. 14)

Quantitative SEM analysis was performed to characterize the morphological features observable at the membrane surface and in the cross-section, namely surface openings, macrovoid architecture, and skin-layer thickness Table 3. It is important to emphasize that SEM does not resolve the intrinsic nanofiltration pores, which are typically in the 1–10 nm range, but rather captures micrometer-scale surface openings and structural features associated with phase inversion phenomena.

CTA2CGLY membranes exhibit a highly porous substructure characterized by long finger-like macrovoids (28 ± 6 μm) and large surface openings (0.42 ± 0.15 μm), indicative of rapid

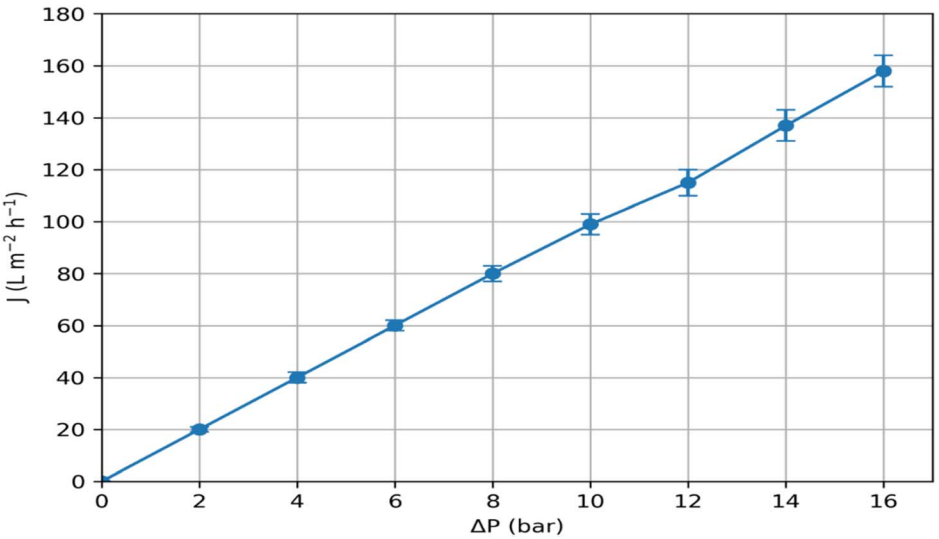

Fig. 15 Pure-water flux of the CTA2CGLY membrane as a function of transmembrane pressure, showing a linear Darcy-type relationship over the 0–16 bar range.

solvent–nonsolvent exchange and instantaneous demixing during immersion precipitation. The dense skin layer remains relatively thin (0.8 ± 0.2 μm), which is favorable for high water permeability but increases the likelihood of non-selective transport pathways.

In contrast, CTA2DGLY membranes show a more compact cross-section, with significantly shorter macrovoids (14 ± 4 μm) and smaller surface openings (0.21 ± 0.08 μm). The thicker and more uniform selective layer (1.6 ± 0.3 μm) reflects delayed demixing and stronger polymer–solvent interactions, which are known to promote better control of the selective barrier in nanofiltration membranes.

Importantly, although the surface openings observed by SEM are in the sub-micrometer range, solute rejection in nanofiltration is governed by the effective free volume and nano-scale transport pathways within the dense skin layer, which typically correspond to equivalent pore sizes below 10 nm, as widely reported for cellulose triacetate-based NF membranes.

Thus, the SEM results primarily provide indirect evidence of transport resistance and selectivity, through skin-layer thickness and structural uniformity, rather than a direct measurement of nanofiltration pore size.

Morphological differences are expected to directly influence transport behavior. The next section examines water permeability as a function of pressure to quantify these effects.

3.10 Water permeability of the CTA2CGLY membrane

Pure-water permeability was measured using a flat-sheet cross-flow filtration cell at 25 ± 1 °C with deionized water. Prior to flux measurements, membranes were pre-compacted at 10 bar for 30–45 min until the flux variation was below 1% over 10 min, ensuring stabilization of the membrane structure. Water flux was then recorded over a transmembrane pressure range of 2–16 bar, with 20 min equilibration at each pressure. All experiments were conducted on five independent membrane coupons ($n = 5$), and the results are reported as mean ± standard deviation.

Hydraulic stability was assessed under continuous filtration at 15 bar. The normalized flux (J/J_0) remained above 0.95 after 8 h of operation, indicating minimal compaction and confirming the mechanical robustness of the CTA membranes under the applied pressures. The linear pressure–flux relationship observed across the entire 0–16 bar range supports a Darcy-type transport regime governed by intrinsic membrane resistance rather than pressure-induced structural deformation.

The CTA2CGLY membrane exhibits a strictly linear increase in pure-water flux (J) with transmembrane pressure (Δp), described by $J = 9.73\ \Delta p + 0.69$ ($R2 = 0.9994$) (Fig. 15). The slope corresponds to a hydraulic permeability Lp ≈ 9.7 L m^{-2} h^{-1} bar^{-1}, while the small positive intercept likely reflects minor experimental bias rather than a true threshold pressure. Such near-ideal linearity is characteristic of membrane-controlled flow through a dense selective layer, where water transport follows Darcy's law and is inversely proportional to the overall hydraulic resistance.[34]

The relatively high permeability of CTA2CGLY can be directly related to the morphological features identified in Section 3.9. SEM analysis revealed a macrovoid-rich substructure and a comparatively thin selective skin layer, which together reduce transport resistance and facilitate convective water flow. It is emphasized, however, that the micrometer-scale surface openings observed by SEM do not represent the intrinsic nanofiltration pores. Instead, water transport and solute separation are governed by nano-scale free volume elements within the dense skin layer, whose effective pore size is typically below 10 nm for CTA-based nanofiltration membranes.

The use of glycerol as a benign pore-former and plasticizer in the CTA casting solution likely contributes to improved hydrophilicity and homogeneous skin formation during phase inversion, thereby promoting stable and reproducible hydraulic performance. This observation is consistent with recent reports employing glycerol derivatives and other bio-based additives to tailor the morphology and permeability of cellulose acetate and cellulose triacetate membranes. In this context, the present results provide a quantitative benchmark for the pressure–flux proportionality of a CTA/glycerol system over an extended pressure window.

Compared with other cellulose-derived nanofiltration membranes reported in the literature, the permeability of CTA2CGLY falls within the range typically observed for dense, unfilled CTA active layers prepared by phase inversion, and remains lower than that of advanced thin-film composite or mixed-matrix designs. This intermediate permeability reflects a deliberate balance between water flux and expected selectivity, making CTA2CGLY a suitable reference membrane for subsequent salt and metal-ion rejection studies.

In contrast, CTA2DGLY membranes, fabricated using dichloromethane, exhibit lower water permeability, consistent with their denser morphology, reduced macrovoid development, and thicker, more uniform selective layer. Although this increased hydraulic resistance limits flux, it is expected to enhance solute rejection through tighter steric hindrance and stronger electrostatic exclusion, as supported by zeta-potential measurements.

Overall, the permeability results, when interpreted in conjunction with SEM-derived morphological parameters, rejection behavior, and surface charge, confirm a strong structure–property–performance relationship. Rapid demixing in chloroform-based systems favors permeability-dominated membranes, whereas delayed phase inversion in dichloromethane-based systems yields selectivity-dominated architectures. This solvent-controlled tunability provides a rational framework for designing CTA nanofiltration membranes targeted toward specific water treatment applications.[35]

3.11 Rejection performance of the CTA2CGLY membrane

The rejection performance of the CTA membranes toward representative mono- and divalent ionic species as a function of applied pressure is presented in Fig. 16. The CTA2CGLY membrane exhibits consistently high rejection of divalent cations (Ca^{2+} and Mg^{2+}) and sulfate anions (SO_4^{2-}), with rejection values exceeding 70% over the investigated pressure range.

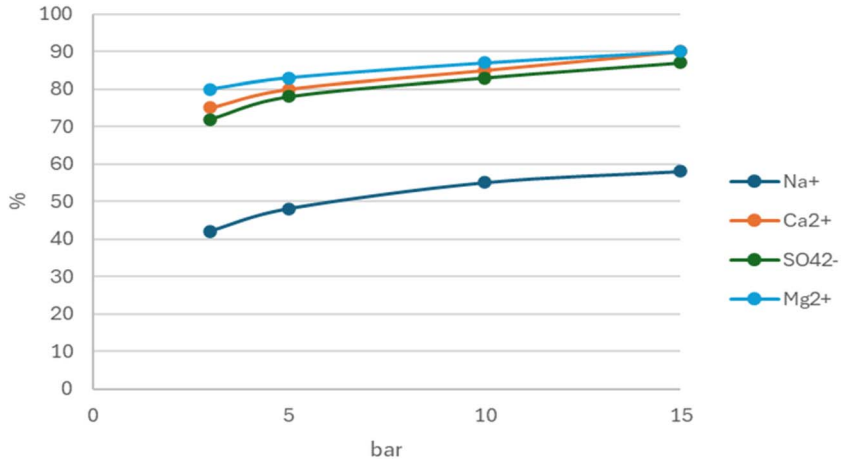

Fig. 16 Rejection of mono- and divalent ions by the CTA2CGLY membrane as a function of applied pressure, illustrating preferential rejection of divalent species characteristic of nanofiltration.

At 15 bar, rejection reaches 89% for Mg^{2+}, 88% for Ca^{2+}, and 87% for SO_4^{2-}, whereas Na^+ rejection remains markedly lower at approximately 58%.

This selective behavior is characteristic of nanofiltration membranes and reflects the combined effects of steric hindrance and electrostatic (Donnan) exclusion, which preferentially limit the transport of multivalent ions relative to monovalent species. The lower rejection of Na^+ is consistent with its smaller hydrated radius and weaker electrostatic interactions, allowing partial permeation through the nanometer-scale free volume elements of the selective layer.

The gradual increase in rejection with applied pressure is primarily attributed to the stabilization of the selective skin layer under operating conditions rather than to significant pressure-induced compaction, as confirmed by the linear Darcy behavior and minimal flux decline discussed in Section 3.10. Under these conditions, increased convective transport accentuates size- and charge-based exclusion without altering the intrinsic membrane structure.

To further quantify selectivity, separation factors (α) were calculated as the ratio of divalent-ion rejection to Na^+ rejection. At 15 bar, Mg^{2+}/Na^+, Ca^{2+}/Na^+, and SO_4^{2-}/Na^+ separation factors of 1.53, 1.52, and 1.50, respectively, were obtained, indicating a clear preferential rejection of divalent species. Notably, the relatively high Mg^{2+} rejection is significant, as Mg^{2+} is often less efficiently rejected by conventional nanofiltration membranes due to its high hydration energy.

The rejection behavior of CTA2CGLY can be rationalized by considering the effective nanofiltration pore size (<10 nm) and the relatively thin selective skin layer identified in Section 3.9. While SEM reveals micrometer-scale surface openings and substructure features, solute separation is governed by nanoscale transport pathways within the dense skin layer. In this membrane, the thinner skin provides moderate steric constraints, allowing partial passage of monovalent ions while

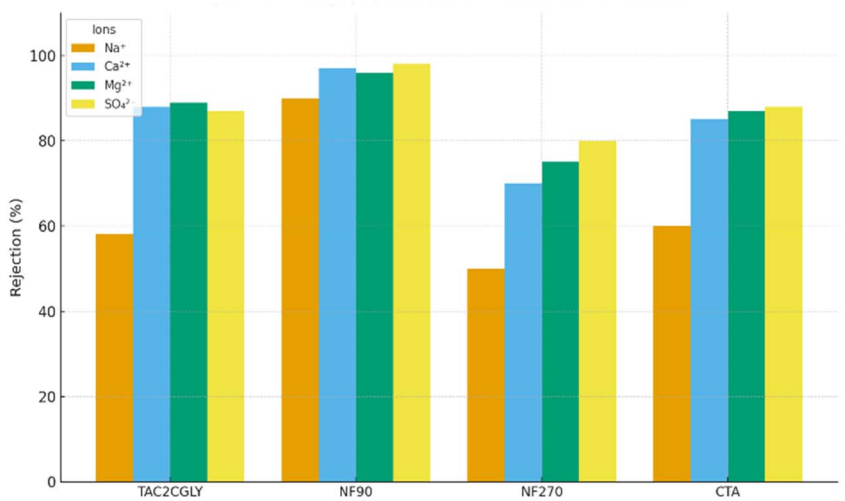

Fig. 17 Comparison of ion rejection performance of CTA2CGLY with commercial nanofiltration membranes (NF90 and NF270) under identical operating conditions.

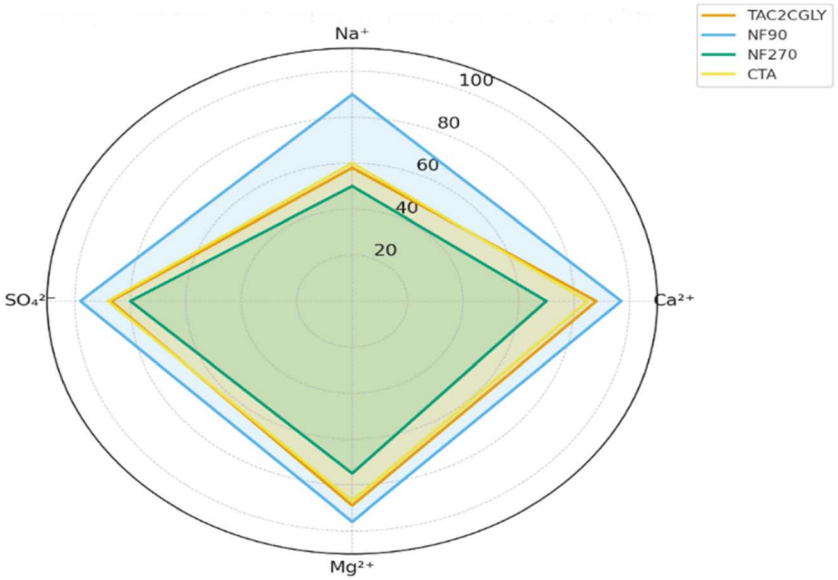

Fig. 18 Radar chart comparing the rejection profiles of CTA2CGLY and commercial nanofiltration membranes toward mono- and divalent ions, highlighting differences in selectivity patterns.

effectively hindering divalent ions with larger hydrated diameters and stronger hydration shells.

Electrostatic effects further reinforce this steric discrimination. Zeta-potential measurements indicate that CTA membranes possess a net negative surface charge over the pH range 3–8. This charge induces Donnan exclusion, which preferentially repels multivalent anions such as SO_4^{2-} and restricts divalent cation transport through electroneutrality constraints. The comparatively weaker negative charge of CTA2CGLY limits electrostatic exclusion of monovalent ions, thereby explaining the observed permeability–selectivity trade-off.

In contrast, CTA2DGLY membranes exhibit higher rejection of multivalent ions, consistent with their thicker and more uniform selective layer and more negative surface charge. The tighter nanofiltration barrier enhances both steric hindrance and electrostatic repulsion, resulting in improved selectivity at the expense of reduced water permeability, as discussed in Section 3.10.

Overall, these results demonstrate that solute rejection in CTA nanofiltration membranes is governed by nano-scale steric and electrostatic mechanisms rather than by SEM-observable surface openings. Solvent-controlled phase inversion effectively tunes skin-layer thickness, effective pore size, and surface charge, enabling rational optimization of the permeability–selectivity balance without modifying the polymer chemistry.

A comparison with commercial NF membranes is presented in Fig. 17 and 18.

While NF90 shows higher Na^+ rejection (>85%), its selectivity for divalent ions is comparable to that of CTA2CGLY. NF270, known for higher permeability but lower selectivity, exhibits weaker divalent ion removal. Interestingly, the CTA2CGLY membrane shows comparable performance to commercial CTA membranes while being derived from agricultural residues, highlighting its potential as a sustainable and cost-effective alternative. Compared to NF270, CTA2CGLY demonstrates superior rejection of divalent ions while maintaining comparable Na^+ rejection. When benchmarked against NF90, the CTA2CGLY membrane exhibits slightly lower monovalent rejection but achieves competitive divalent rejection. Importantly, the performance is in line with CTA membranes, which reinforces the relevance of millet husk-derived CTA as a green alternative for nanofiltration.

The radar chart (Fig. 18) provides an integrated visualization of the rejection performance of the studied and commercial membranes.

The CTA2CGLY membrane shows a rejection profile that closely overlaps with that of commercial CTA membranes, particularly for divalent ions (Ca^{2+} and Mg^{2+}) and sulfate, confirming its strong potential as a bio-based substitute. In contrast, NF90 exhibits a nearly full polygon, reflecting its superior rejection across all ions, including Na^+, which is consistent with its dense structure and lower water permeability. NF270 displays a smaller polygon area, emphasizing its lower selectivity and higher permeability, which make it suitable for applications requiring partial salt passage. The radar chart thus highlights the balanced performance of CTA2CGLY, combining adequate Na^+ rejection with high selectivity for divalent ions, a behavior highly desirable for water softening and sulfate removal in brackish water treatment. This graphical comparison reinforces that membranes derived from agricultural residues can achieve competitive performance relative to established commercial NF membranes, while offering the additional advantage of sustainability.

Taken together, these results highlight the critical role of biomass composition, acetylation chemistry, solvent selection, and interfacial charge in shaping membrane performance. The concluding section synthesizes these insights and outlines perspectives for scaling and application.

4 Conclusion and perspectives

This work demonstrates a comprehensive structure–property–performance relationship for nanofiltration membranes fabricated from millet husk–derived cellulose triacetate. By coupling controlled acetylation chemistry with solvent-engineered phase inversion, it is shown that membrane morphology, pore size distribution, and surface charge can be finely tuned without modifying the polymer backbone. Quantitative SEM and electrokinetic analyses reveal that solvent choice governs the balance between steric hindrance and electrostatic (Donnan) exclusion, which together dictate ion-rejection behaviour. Chloroform-based membranes provide an optimal compromise between permeability and selectivity through broader pore distributions and moderate negative surface charge, while dichloromethane promotes denser skins and stronger electrostatic exclusion.

Beyond performance metrics, the originality of this study lies in the integrated valorisation of millet husk, the explicit mechanistic linking of solvent-driven morphology to steric and electrostatic rejection, and the demonstration that bio-sourced CTA membranes can rival commercial NF materials. These findings position millet husk–derived CTA membranes as a promising, sustainable alternative for water softening, sulfate removal, and industrial wastewater treatment, particularly in regions where agricultural residues are abundant. The approach provides a scalable and environmentally conscious pathway for advancing circular bioeconomy-based membrane technologies. Future research should aim at:

•Scaling up production by optimizing casting protocols and solvent systems while considering greener, less toxic alternatives to chlorinated solvents.

•Improving long-term stability through surface modification (*e.g.*, grafting of antifouling agents, nanofillers, or interlayers) to mitigate fouling and scaling in real water matrices.

•Extending application fields, particularly in brackish water softening, industrial wastewater treatment (textile effluents and mining discharges), and selective removal of heavy metals, where high divalent ion rejection is advantageous.

•Life-cycle assessment (LCA) to quantify environmental and economic benefits of millet husk valorization compared to fossil-based polymers, thereby strengthening the case for circular bioeconomy models in Sub-Saharan Africa.

Integration in hybrid systems, coupling CTA-based NF membranes with advanced oxidation, microbial fuel cells, or electrodialysis, to enhance contaminant removal and energy efficiency.

By addressing these avenues, millet husk–derived CTA membranes could significantly contribute to the development of sustainable, locally sourced, and cost-effective water treatment technologies adapted to the challenges of developing regions.

Author contributions

Mouhamed Ndoye: investigation, methodology data curation, writing–original draft; El Hadji Moussa Diop: formal analysis, software, validation, supervision, writing–review & editing; Moustapha Sène: formal analysis, writing–review & editing; Maryam Khadim MBACKE: conceptualization, project administration, validation, supervision, writing–original draft.

Conflicts of interest

The authors have no relevant financial or non-financial interests to disclose.

Data availability

The data supporting the findings of this study are available in the article and its supporting information (SI). Further information is also available on request from the corresponding author. Supplementary information: the preparation and optimization of nanofiltration membranes based on cellulose triacetate (CTA) derived from millet husk. It describes the formulation of polymer casting solutions, the selection of suitable solvents and plasticizers, and membrane fabrication via non-solvent induced phase separation. Three preparation protocols were evaluated using different solvent systems (acetone, dichloromethane, and chloroform) and plasticizers (glycerol and PEG 600). Chloroform/glycerol-based formulations were identified as the most suitable, yielding homogeneous casting solutions and membranes with satisfactory morphology and mechanical integrity. Optimized processing conditions and repeatability tests are also reported, demonstrating the robustness of the selected protocol. See DOI: https://doi.org/10.1039/d5su00889a.

Acknowledgements

Our thanks to Professor Anthony SZYMCZYK and the entire Chemistry and Process Engineering research team for welcoming us to the Institute of Chemical Sciences of Rennes (UMR CNRS 6226), as part of this work.

References

1 M. Kadhom and B. Deng, Metal-organic frameworks (MOFs) in water filtration membranes for desalination and other applications, *Appl. Mater. Today*, 2018, **11**, 219.
2 D. Lu, T. Ma, S. Lin, Z. Zhou, Ge Li, Q. An, Z. Yao, S. Qi, Z. Sun and Z. Lin, Constructing a selective Blocked-nanolayer on nanofiltration membrane via surface-charge inversion for promoting Li+ permselectivity over Mg^{2+}, *J. Membr. Sci.*, 2021, **635**, 119504.
3 Z. Geng, X. Yu Wang, H. Jiang, L. Zhang, C. Zhiting, Y. Feng, W. Geng, X. Yang, M. Huo and S. Jing, High-Performance TiO2 Nanotubes/Poly(aryl ether sulfone) Hybrid Self-Cleaning Anti-Fouling Ultrafiltration Membranes, *Polymers*, 2019, **11**, 555.
4 H. Lee, D. Segets, S. Süß, W. Peukert, S. S. C. Chen and D. Y. H. Pui, Effects of filter structure, flow velocity, particle concentration and fouling on the retention efficiency of ultrafiltration for sub-20 nm gold nanoparticles, *Sep. Purif. Technol.*, 2020, **241**, 116689.
5 O. O. Sadare, K. O. Yoro, K. Moothi and M. O. Daramola, Lignocellulosic Biomass-Derived Nanocellulose Crystals as Fillers in Membranes for Water and Wastewater Treatment: A Review, *Membranes*, 2022, **12**, 320.

6 A. Saud, H. Saleem and S. J. Zaidi, Progress and Prospects of Nanocellulose-Based Membranes for Desalination and Water Treatment, *Membranes*, 2022, **12**, 462.
7 A. Barhoum, K. U. Deshmukh, M.- Luisa García-Betancourt, S. Alibakhshi, S. Mohadeseh Mousavi, A. Meftahi, M. S. K. Sabery and P. Samyn, Nanocelluloses as sustainable membrane materials for separation and filtration technologies: Principles, opportunities, and challenges, *Carbohydr. Polym.*, 2023, **317**, 121057.
8 Md. Didarul Islam, F. Jalal Uddin, T. Ur Rashid and M. Shahruzzaman, Cellulose acetate-based membrane for wastewater treatment—A state-of-the-art review, *Mater. Adv.*, 2023, **18**, 4054–4102.
9 J. Wang, S. Comail Abbas, L. Li, C. C. Walker, Y. Ni and Z. Cai, Cellulose Membranes: Synthesis and Applications for Water and Gas Separation and Purification, *Membranes*, 2024, **14**, 148.
10 R. Das, T. Lindström, M. Khan, aM. Rezaei and B. S. Hsiao, Nanocellulose preparation from diverse plant feedstocks, processes, and chemical treatments: A review emphasizing non-woods, *BioResources*, 2023, **19**, 1865–1924.
11 M. L. Hassan, S. M. Fadel, R. E. Abouzeid, W. S. Abou Elseoud, E. A. Hassan, L. Berglund and K. Oksman, Water purification ultrafiltration membranes using nanofibers from unbleached and bleached rice straw, *Sci. Rep.*, 2020, **10**, 11278.
12 H.-F. Tan, B. S. Ooi and C. P. Leo, Future perspectives of nanocellulose-based membrane for water treatment, *J. Water Proc. Eng.*, 2020, **37**, 101502.
13 M. Yang, P. Hadi, X. Yin, J. Yu, X. Huang, H. Ma, H. W. Walker and B. S. Hsiao, Antifouling nanocellulose membranes: How subtle adjustment of surface charge lead to self-cleaning property, *J. Membr. Sci.*, 2021, **618**, 118739.
14 A. I. Osman, M. Nasr, M. Farghali, S. S. Bakr, A. S. Eltaweil, A. K. Rashwan and E. M. Abd El-Monaem, Machine learning for membrane design in energy production, gas separation, and water treatment: a review, *Environ. Chem. Lett.*, 2024, **22**, 505–560.
15 G. A. Bastida, R. J. Aguado, M. V. Galván, M. Á. Zanuttini, M. Delgado-Aguilar and Q. Tarrés, Impact of cellulose nanofibers on cellulose acetate membrane performance, *Cellulose*, 2024, **31**, 2221–2238.
16 B. T. Akinyemi, O. D. Ogundele and A. B. Afolabi, Advancements in Sustainable Membrane Technologies for Enhanced Remediation and Wastewater Treatment: A Comprehensive Review, *Acadlore Trans. Geosci.*, 2023, **2**, 196–207.
17 T. Ahmed, E. Mohamed, M. N. Khalil, A. I. Osman and D. W. Rooney, Sulfonated graphene nanomaterials for membrane antifouling, pollutant removal, and production of chemicals from biomass: a review, *Environ. Chem. Lett.*, 2022, **21**, 1093–1116.
18 H. Idress, S. Z. J. Zaidi, A. Sabir, M. Shafiq, R. U. Khan, C. Harito, S. Hassan and F. C. Walsh, Cellulose acetate based Complexation-NF membranes for the removal of Pb(II) from waste water, *Sci. Rep.*, 2021, **11**, 1806.
19 Ç.- Emecen, F. Seden Tekin and P. Zeynep, Controlling Cellulose Membrane Performance via Solvent Choice during Precursor Membrane Formation, *ACS Appl. Polym. Mater.*, 2023, **5**, 2185–2194.
20 R. Cang Sun, J. Tomkinson, P. L. Ma and S. F. Liang, Comparative study of hemicelluloses from rice straw by alkali and hydrogen peroxide treatments, *Carbohydr. Polym.*, 2000, **42**, 111–122.
21 A. Sluiter, B. Hames, R. Ruiz, C. Scarlata, J. Sluiter, D. Templeton, & D. Crocker, Determination of structural carbohydrates and lignin in biomass, National Renewable Energy Laboratory, (NREL/TP-510-42618), 2012.
22 P. Binod, R. Sindhu, R. R. Singhania, S. Vikram, L. Devi, S. Nagalakshmi, N. Kurien, R. K. Sukumaran and A. Pandey, Bioethanol production from rice straw: An overview, *Bioresour. Technol.*, 2010, **101**, 4767–4774.
23 P. Kumar, D. M. Barrett, M. J. Delwiche and P. Stroeve, Methods for pretreatment of lignocellulosic biomass for efficient hydrolysis and biofuel production, *Ind. Eng. Chem. Res.*, 2009, **48**, 3713–3729.
24 V. Menon and M. Rao, Trends in bioconversion of lignocellulose: Biofuels, platform chemicals & biorefinery concept, *Prog. Energy Combust. Sci.*, 2012, **38**, 522–550.
25 H. M. Shaikh, A. Anis and A. M. Poulose, Synthesis and Characterization of Cellulose Triacetate Obtained from Date Palm (Phoenix dactylifera L.) Trunk Mesh-Derived Cellulose, *Molecules*, 2022, **27**, 1434.
26 H. Dirk, J. Puls and S. A. Wilson, Degradation of Cellulose Acetate-Based Materials: A Review, *J. Polym. Environ.*, 2011, **19**, 152–165.
27 T. Azi, A. Farid, F. Haq, M. Kiran and A. Ullah, A Review on the Modification of Cellulose and Its Applications, *Polymers*, 2022, **14**, 3206.
28 A. E. Childress and M. Elimelech, Effect of Solution Chemistry on the Surface Charge of Polymeric Reverse Osmosis and Nanofiltration Membranes, *J. Membr. Sci.*, 1996, **119**, 253–268.
29 P. Fievet, M. Sbaï, A. Szymczyk and A. Vidonne, Determining the ζ-potential of plane membranes from tangential streaming potential measurements: effect of the membrane body conductance, *J. Membr. Sci.*, 2003, **226**, 227–236.
30 S. Acarer-Arat, İ. Pir, M. Tüfekci, S. Güneş-Durak, A. Akman and N. Tüfekci, Heavy Metal Rejection Performance and Mechanical Performance of Cellulose-Nanofibril-Reinforced Cellulose Acetate Membranes, *ACS Omega*, 2024, **9**, 42159–42171.
31 X. Dong, D. Lu, T. A. L. Harris and I. C. Escobar, Polymers and Solvents Used in Membrane Fabrication: A Review Focusing on Sustainable Membrane Development, *Membr.*, 2021, **11**, 309.
32 K. T. Rashid, H. M. Alayan, A. E. Mahdi, M. N. AL-Baiati, H. S. Majdi, I. K. Salih, J. M. Ali and Q. F. Alsalhy, Novel Water-Soluble Poly(terephthalic-co-glycerol-g-fumaric acid) Copolymer Nanoparticles Harnessed as Pore Formers for Polyethersulfone Membrane Modification: Permeability–Selectivity Tradeoff Manipulation, *Water*, 2022, **14**, 1507.
33 F. S. Tekin and P. Z. Çulfaz-Emecen, Controlling Cellulose Membrane Performance via Solvent Choice during

Precursor Membrane Formation, *ACS Appl. Polym. Mater.*, 2023, **5**, 2185–2194.

34 A. Piry, A. Heino, W. Kühnl, T. Grein, S. Ripperger and U. Kulozik, Effect of membrane length, membrane resistance, and filtration conditions on the fractionation of milk proteins by microfiltration, *J. Dairy Sci.*, 2012, **95**, 1590–1602.

35 M. A. Rasool and I. F. J. Vankelecom, Preparation of full-bio-based nanofiltration membranes, *J. Membr. Sci.*, 2021, **618**, 118674.